2019-05-01

Segmentation And Registration Based Automatic Cancer Proton Treatment Analysis

Yang Zhang
University of Texas at El Paso, zybf1208@gmail.com

SEGMENTATION AND REGISTRATION BASED AUTOMATIC CANCER PROTON TREATMENT ANALYSIS

YANG ZHANG

Doctoral Program in Biomedical Engineering

APPROVED:

Wei Qian, Ph.D., Chair

Jianying Zhang, M.D,Ph.D.

Thomas Boland, Ph.D.

Sergio D. Cabrera, Ph.D.

Charles H. Ambler, Ph.D.
Dean of the Graduate School

To my parents

I feel lucky to have a supportive family. Thank you for giving me life and raising me well. I appreciate you two more than you will ever know and I love you always.

SEGMENTATION AND REGISTRATION BASED AUTOMATIC CANCER PROTON TREATMENT ANALYSIS

By

YANG ZHANG,M,S.

DISSERTATION

Presented to the Faculty of the Graduate School of

The University of Texas at El Paso

in Partial Fulfillment

of the Requirements

for the Degree of

DOCTOR OF PHILOSOPHY

Department of Metallurgical, Materials and Biomedical Engineering

THE UNIVERSITY OF TEXAS AT EL PASO

May 2019

Acknowledgments

I would like to express my utmost appreciation for my mentor, Dr. Wei Qian: You are the wisest and most farsighted professor I have ever met and you have always provided me with invaluable suggestions to help me overcome any obstacles, both in research and in life. I would like to acknowledge and extend my heartfelt gratitude to my committee members, Dr. Zhang and Dr. Boland. Thank you for introducing and admitting me to the Biomedical Engineering Program at UTEP. I firmly believe that this has been the greatest opportunity that has ever been given to me.

I also want to include Dr. Sahoo, a professor in the Department of Radiation Physics at the MD Anderson Cancer Center. Thank you for sharing your extensive knowledge of proton therapy. I feel so fortunate to be able to learn from you, an expert in the field. You are the most widely respected proton physicist in the world.

Lastly, I feel lucky to have a supportive family. Thank you to my parents for giving me life and raising me well. I appreciate you two more than you will ever know and I love you always. Thank you to all my friends, who have consistently believed in me and have supported me throughout my journey. I have learned much from you!

Nomenclature

3D: Three-dimensional

CTC: Circulating Tumor Cell, a tumor cell which is shed from the tumor or metastasis then enters the bloodstream.

CT: Computed Tomography

CK: Cytokeratin is an intermediate filament expressed by epithelial cells which is used in this project to tag CTC.

CD45: A differentiation that shows an extracellular protein expressed by leukocytes, used to tag both neutrophils and leukocytes.

DTA: Distance-to-agreement

DAPI: 40, 6-diamidino-2-phenylindole (a nuclear stain)

EpCAM: Epithelial Cellular Adhesion Molecule, is an extracellular marker expressed by epithelial cells which is used in this project to capture CTC.

IDD: Integral depth dose

IMRT: Intensity-Modulated Radiation Therapy

SSD: Source Surface Distance

TPS: Treatment planning system

WET: Water-equivalent thickness

SSPT: Spot scanning proton therapy

Abstract

Due to its low side effects, proton therapy is rapidly developing around the world. However, the time and labor it takes to deliver the treatment have prevented widespread use in the clinic setting. For this reason, an automatic proton treatment analysis system is needed to improve efficiency during the treatment process.

The challenge lies in improving the accuracy and speed of the current proton treatment analysis system. The Range shifter correction factor is considered the same value under any given condition in our treatment system. This approximate algorithm limits the accuracy of the proton treatment analysis system. In addition, medical professionals spend a great deal of time checking for errors. Errors, such as contouring mistakes and unnecessary spots are manually reviewed during the treatment plans analysis process. At present, the dose calculation engine in the analysis system requires five hours to complete one treatment plan. The calculation speed limits our treatment capacity. Because the status of a tumor changes over the duration of the treatment process, monitoring its status is imperative for delivering an accurate dosage. Our research involves the development of an automatic proton treatment analysis system that uses methods based on segmentation and registration algorithms to solve these problems.

The automatic proton treatment analysis system (and the accuracy and speed at which it operates) has been validated in a clinical setting. Therefore, this analysis system could potentially replace manual operation during the proton treatment plan quality assurance process. The amount of time it takes to deliver proton therapy will be significantly reduced.

Table of Contents

List of Figures

List of Tables

1 Introduction

1.1 Fundamentals Of Proton Therapy

Cancer is the principal cause of death in the United States, second to heart disease. In 2013 it was reported that in the United States alone, 1,660,290 individuals were diagnosed and 580,350 individuals died from cancer related illness[1]. Radiation therapy is one of the main methods used in treating cancer. Proton therapy is a type of radiation therapy. It is a treatment that uses high-energy proton beams to treat tumors[2].

1.1.1 History Of Proton Beam Radiotherapy

In 1946, Robert R. Wilson was the first researcher to propose the use of protons for radiation therapy at the Harvard Cyclotron Laboratory [3].The first patient was treated at Lawrence Berkeley Laboratory in 1954. The Particle Therapy Cooperative Group (PTCOG) reports that annually, about 55,000 patients worldwide are treated with proton therapy. This includes about 18,000 patients in the United States, where only five facilities exist for treatment. Internationally, the number of operational and pending proton therapy centers is listed at around 50[4].

1.1.2 Physical Rationale

A proton is a particle that carries a positive charge. Protons can deposit energy into the matter they pass through via ionization. From a radiobiological perspective, this imparted energy can damage the DNA of cells. Toxic DNA lesions result in base and sugar modifications, single-strand breaks, and double-strand breaks[5]. Damaged DNA may result in the cessation of cell division.

The main reason a proton beam is considered therapeutic for the treatment of tumors is because protons have a well-defined penetration range. This advantage of proton therapy compared to traditional radiation therapy has to do with the proton beam: It conforms to the tumor three-dimensionally in a much better way[6]. As the proton transports through human tissue, it slows down by interaction with electrons and loses energy. The point at which the highest energy of deposit happens is called the "Bragg peak" (Figure 1.1)[7]. Physicians want the Bragg peak's location to coincide with the tumor mass, thus directing the most energy towards killing tumor cells.

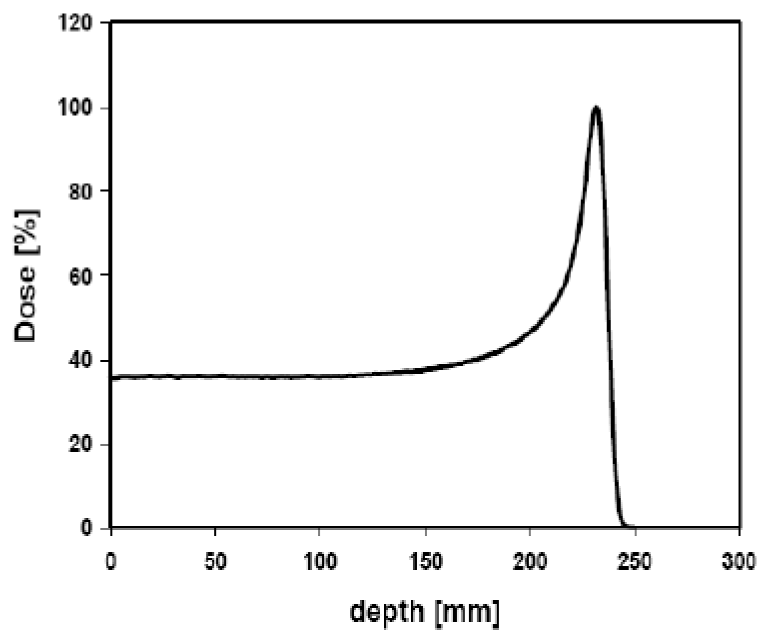

Figure 1.1 Depth-Dose distribution of a broad proton beam in water[7]

1.1.3 Treatment Planning System

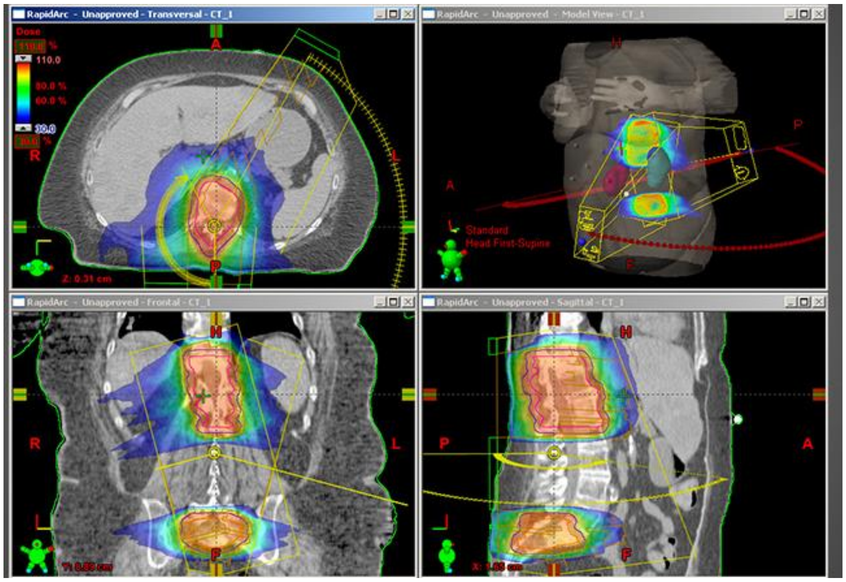

Figure 1.2 Eclipse treatment planning system[8]

The Treatment Planning System (TPS) is a key part of proton therapy. Oncologists will identify tumors from the images presented in the system (Figure 1.2). The system will develop a plan for delivering proton beams to the tumors based on beam line routes. TPS also calculates the expected dose distribution in the patient's tissue. Critical structures of the human body could be protected by optimized beam placement. These beam routes are calculated via complex programs[9]such as the Eclipse Treatment Planning System (Eclipse: Version 8.917 by Varian Medical Systems, Palo Alto, CA). Eclipse is the commercial TPS used at the MD Anderson Cancer Center. The calculation method of the system is a trade secret. Our proton treatment analysis system will implement the type of quality assurance necessary for proton treatment plans created by the TPS.

1.1.4 MD Anderson Cancer Center Proton Therapy Facility

MD Anderson Cancer Center proton-therapy facility consists of three main components: an accelerator with an energy selection system, a beam transport system, and a beam delivery system (Figure 1.3).

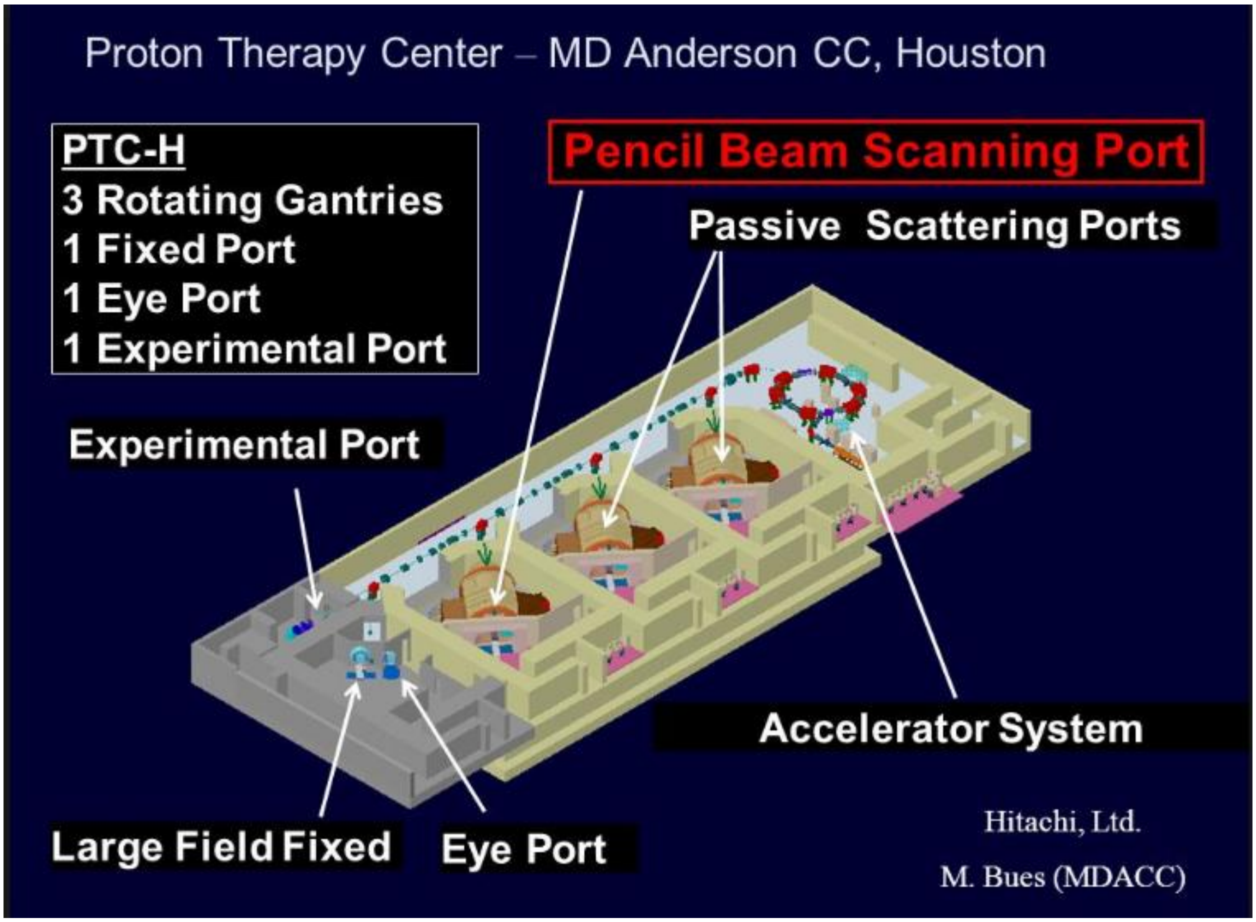

Figure 1.3 Proton Therapy Center-MD Anderson Cancer Center, Houston[10]

Protons are generated inside the accelerator and sent out via the beam delivery system. At the source of the accelerator, hydrogen atoms are divided into electrons carrying a negative charge and protons with a positive charge[11]. The protons are then shot through a vacuum tube into a linear accelerator, where the energy increases to 7 million electron volts per microsecond. To acquire the range of depth necessary for the proton to be delivered, proton beams accelerate to 70 to 250 million electron volts before being sent out from the synchrotron. A series of magnets in the beam delivery system will guide the protons to move in the assigned direction, focusing on the appropriate treatment area [12]. A Gantry revolving 360 degrees could deliver the beam to the patient from any angle (Figure 1.4). There are a series of software and hardware control systems used to implement the whole system (Figure 1.3).

Figure 1.4 MD Anderson proton delivery system

1.1.5 TOPAS: Particles Simulation Tool

TOPAS is used to make advanced particle simulation of all forms of radiotherapy. It is applied to model proton treatment plans in this research. We were able to configure pre-built components (such as nozzles, patient geometry, dosimetry, range shifter, and imaging components) to simulate proton treatment using TOPAS [13]. Dose distribution matrices for the range correction factor in Chapter 2 and fast dose calculations in Chapter 3 were acquired by simulation of the TOPAS.

1.1.6 Matrixx: Standard Clinical Dose Measurement Device

Matrixx (MatriXXTM, ScanditronixWellhofer, Schwarzenbruck, German) [14] is a proton dose measurement device. All of the clinical dose measurements in this dissertation are implemented by Matrixx (created by IBA Dosimetry). MatriXX is a two-dimensional array of 1020 (32×32) vented, parallel plate pixeled ion chambers. Each chamber has a diameter of 4.5 mm and a sensitive volume of 0.08 cc. The center-to-center separation between the chambers is 7.62 mm, and the active field size is 24×24 cm^2.

1.2 Fundamentals Of Circulating Tumor Cells Isolation Technology

Circulation tumor cells (CTCs) detection and isolation method will be used to monitor tumor status in guiding proton treatment. The concept of CTCs and CTCs isolation device we used will be introduced as follows.

1.2.1 Circulating Tumor Cell

Metastasis is the main cause of cancer-related death in patients with solid tumors [14] . Circulating Tumor Cell (CTC) is a tumor cell which is shed from the tumor, then enters the bloodstream (Figure 1.5). CTC is regarded as key in interpreting cancer metastasis since CTC can potentially provide information about the different cancers and mechanisms of metastasis[15] . Increasing evidence suggests that CTC monitoring could guide tumor treatment [16] [17] . Furthermore, the heterogeneous nature of CTCs provides inclusive, non-invasive means for characterizing tumor molecular subtypes such as phenotype. Genetic information can be used to provide critical information used to guide cancer treatment [18, 19]. Circulating cancer cells are detected in common epithelial cancers, including breast, prostate, and lung [20].

Cytokeratins, prostate-specific antigen (PSA), mucin-1 (MUC-1), HER2, AFP (-fetoprotein), and the CEA (carcinoembryonic antigen) gene family among others are used as tumor cell–specific markers [21].

Figure 1.5 Schematic view of the metastatic process showing CTC transit: the CTCs exit the primary tumor, intrastate into the bloodstream, circulate, and extravagate into a secondary site where they may ultimately achieve different fates including dormancy and full-blown metastasis. [22] . Nature Publishing Group.

1.2.2 NanoVelcro Cell-affinity Substrates: CTCs Isolation Device

Circulating tumor cells can be isolated during the process of metastasis. Because CTCs are tremendously rare (there is approximately one CTC per billion normal blood cells circulating in patients with advanced cancer[23]), the enrichment of CTC is a very important step in the detection procedure. Motivated by nanoscale interactions observed in the tissue microenvironment, nanosubstrates (CTC captured, agent-coated, nanostructured substrates) were utilized to restrain CTCs with high efficiency. The working mechanism in NanoVelcro cell-affinity substrates describes the relationship between a cell surface antigen and a nano surface antigen. When both are tangled together, strong binding occurs and the cell is captured [24] . Figure 1.6 shows the principle of the chip. CTCs can be enriched on the chip after most blood cells are removed by solution fluid. More information about nanosubstrate system is introduced in reference [23].

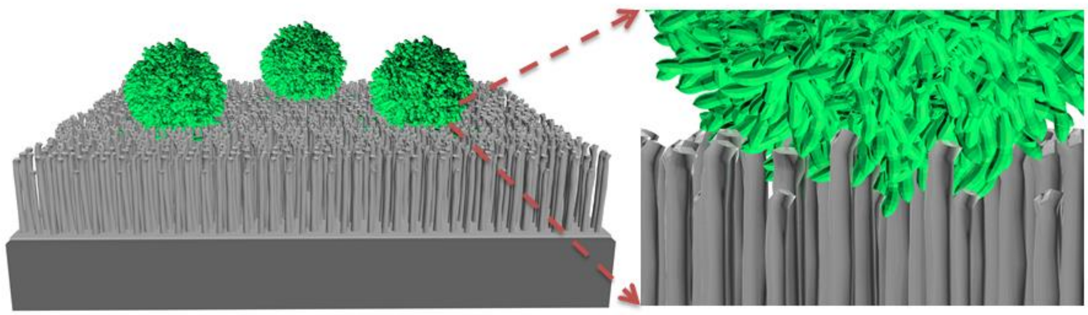

Figure 1.6 Nano cell-affinity substrates working mechanism [23]

1.3 Scope Of Dissertation

This dissertation will summarize our current research and describe the automatic proton treatment analysis system step by step (Figure 1.7).

Chapter 2 will provide information about the range shifter correction factor and apply the correction factor data set to proton treatment plans, showing improvement in dose calculation accuracy of the proton treatment analysis system. (Figure 1.7 (1)).

Chapter 3 will introduce the concept of small spot clusters and apply an analytical method toward the detection of errors in treatment plans, thereby replacing manual detection and improving the work efficiency of medical professionals (Figure 1.7 (2)).

Chapter 4 will provide a fast dose calculation algorithm to implement high speed dose calculations. The calculation results will be used for quality assurance (Figure 1.7(3)).

Chapter 5 provides an automatic CTC analysis program. This CTCs detection and isolation method could be used for monitoring the status of tumors, in which results could be used to guide the proton treatment process (Figure 1.7(4)).

Chapter 6 will summarize this research and discuss the future research plan.

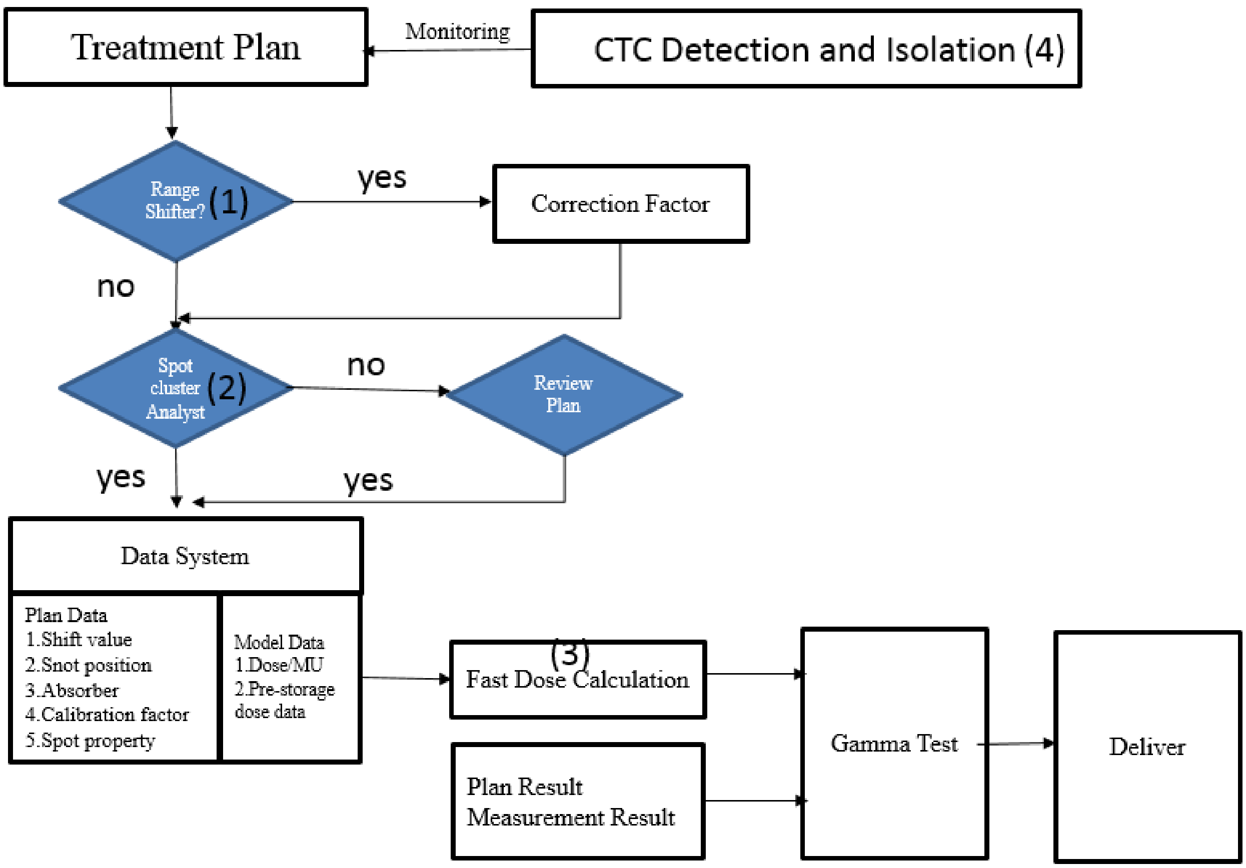

Figure 1.7 Automatic proton treatment analysis system

2 Dose Calculation For Scanning Spot Proton Therapy With Application Of Range Shifter

2.1 Abstract

Purpose: A correction factor data set is built to improve dose calculation quality for proton treatment analysis system that makes use of a range shifter, sometimes called an energy absorber.

Material And Method: The particle simulation tool TOPAS was used to simulate the range shifter model for correction factor calculation. A range shifter, Bragg peak chamber, and water scanning system were used to validate the correction factor method. The synchrotron-based spot scanning proton therapy system has an energy range of 72.5 to 221.8 MeV. A brain case treatment plan was used to demonstrate the clinical significance of the correction factor data set.

Result: The beam parameters in simulations were finely tuned to make the simulated dose distributions match the measurements with the mean difference in the magnitude of 1.0%. The TOPAS generated correction factors for different beam energies and different depths in the water phantom show that for each specific beam energy the dose correction factor increases with the increase of air gap and decreases with the increase of depth in water, and larger correction factors are needed for higher beam energies. The gamma test pass rate for the selected brain treatment plan was improved from 80.4% to 97.8% after applying the dose correction factors.

Conclusion: The range shifter correction factor data set is a practical, low-cost solution that could significantly improve the dose calculation accuracy for SSPT clinics.

2.2 Introduction

Spot scanning proton therapy (SSPT) is used to deliver intensity-modulated proton therapy (IMPT) in MD Anderson Cancer Center. The three-dimensional volume of the tumor target is dynamically scanned by, sort of, painting the target with proton Bragg peaks layer-by-layer [25, 26]. Two scanning magnets are used to control the lateral beam position (X and Y) and variable energies of protons extracted from the synchrotron are applied to control the depth (Z). All layers are scanned sequentially from the highest to the lowest energy, that is, from the distal edge to the proximal edge of the tumor target.

The synchrotron-based SSPT beam delivery system (PROBEAT Proton Beam Therapy System, Hitachi America, Ltd., Tarrytown, NY, USA) at the University of Texas M. D. Anderson Cancer Center Proton Therapy Center in Houston, Texas (PTCH) can produce 94 energies ranging from 72.5 MeV to 221.8 MeV, corresponding to proton ranges of 4.0–30.6 cm in water[25] and similar ranges for other materials based on their water-equivalent thickness (WET). The maximum field size is 30 × 30 cm^2 at isocenter. For patients with targets shallower than 4.0 cm WET, a range shifter (sometimes called an energy absorber) is used to reduce the range of higher energy beams to the desired range, as shallow as 0.3 cm WET. Besides, a high-energy beam has a relative small spot size; therefore, using range shifters and high-energy beams together can reduce the dose penumbra to the desired locations in the targets [12]**.** The range shifter used at PTCH is made of ABS (Acrylonitrile butadiene styrene) resin (ρ = 1.04 g/cm^3) and has a WET of 6.7 cm. **(**Figure 2.1.A**)** [12]. For the PTCH system, the range shifter is placed at the distalmost edge of the beam nozzle (Figure 2.1.A). The nozzle, along with the range shifter, can be extended along the beam direction, allowing the distal edge of the nozzle to have a position anywhere from isocenter to 38 cm proximal to isocenter. In this paper, air gap is defined as the distance from the range shifter distal surface to target's proximal surface as shown in Figure 2.1A. The air gap changes as range shifter position changes, assuming the target position stays fixed.

In our clinical practice, we found that the dose calculation accuracy of the treatment planning system (TPS) for treatment plans using the range shifter is lower than the average accuracy of all treatment plans [27]. We found that the dose delivered to the target, for a given depth and beam energy, varies with air gap (the distance between the range shifter distal surface and target proximal surface (Figure 2.1B). To our knowledge, this topic has seldom been discussed previously in the literature. It seems that until now, the TPS and other dose engines, have simply assumed an air gap of 0 [28, 29]. This deficiency of the dose calculation algorithm caused noticeable discrepancies in patient-specific quality assurance results. In this paper we propose to build a correction factor data set for a higher accuracy dose calculation.

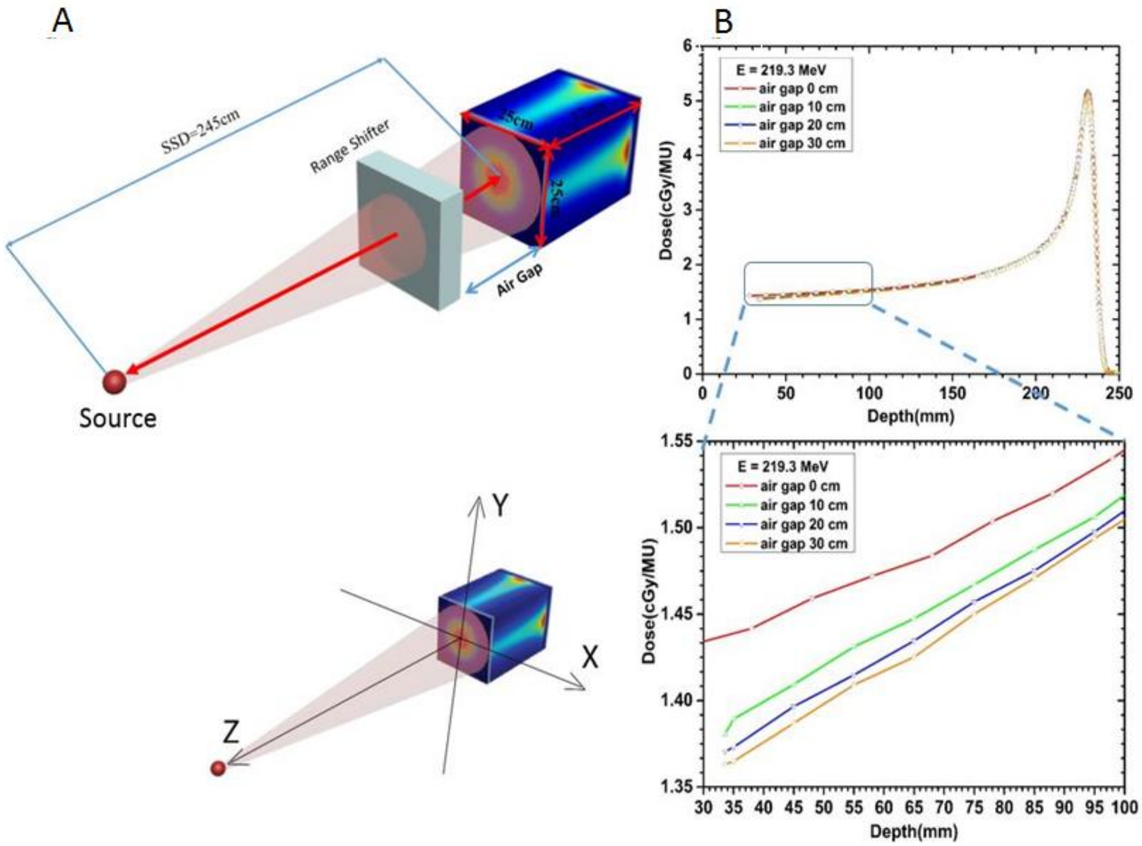

Figure 2.1 (A) Illustration of IDD measurements with different air gaps between the range shifter and the water phantom. (B) The measured IDD distributions in water for 219.3 MeV protons with air-gap sizes of 0 cm, 10 cm, 20 cm and 30 cm. The enlarged view in the bottom panel shows the differences with different air-gap sizes. The Bragg peak chamber (scoring radius = 4.08 cm) was used to perform the IDD measurements along the z axis.

2.3 Method and Materials

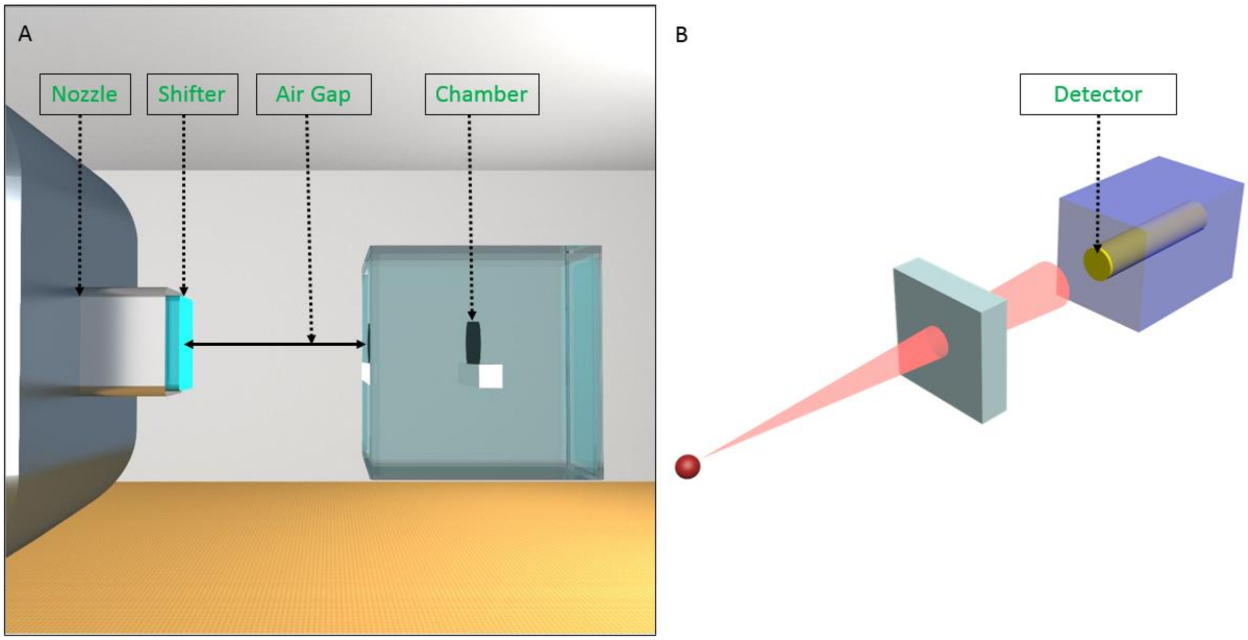

Figure 2.2 (A) Setup of the IDD measurements. The range shifter is mounted on the snout of the scanning proton nozzle. The snout can be retracted and extended to provide different air-gap sizes between the range shifter and the water phantom. The Bragg peak chamber is positioned along the central axis. It is mounted on the automatic scanning system of the water tank to measure dose at different locations. (B) The setup used in TOPAS simulations. Two different types of virtual detectors are built. A cylinder with radius of 4.08 cm and thickness of 1 mm is used to model the Bragg peak chamber. Because the spot sizes of low-energy beams are larger than the size of the Bragg peak chamber. A larger layer of 25 cm * 25 cm * 1 mm is modeled as a sensitive detector to capture most of the transporting particles.

2.3.1 Evaluation And Simulation Tools

2.3.1.1 Gamma test: Dosage calculation validation method

The gamma test is applied to validate the accuracy of dosage calculation results used in proton therapy. It is also used to validate the accuracy of the range shifter correction factor and the fast dose calculation algorithm presented in this dissertation.

Gamma test can assess dosage distributions through a composite analysis of distance-to-agreement (DTA) and difference in dose amounts [30]. The technique integrates both DTA and dose difference analysis and provides a numerical gamma index as an evaluation value of the agreement between two datasets.

Range uncertainties in the delivery of proton therapy result from both the conversion of computed tomography (CT) in Hounsfield units to proton stopping power [31] and image artefacts [6]. Therefore, an uncertainty of approximately ±3% is considered in our clinical practice[32]. The standard for the gamma test is equal to 90% of the testing points passed based on a 3 mm distance to agreement and a 3% difference in dose amount.

The pass rate of Gamma test stands for the difference between measurements data (r_m) for each reference point and calculation data (r_c). The value is usually scaled to acquire dimensionless quantitates. In this paper the value is set as 3 mm-3%, which means the specific point is within 3 mm in comparison to the reference point and dose difference is within 3%. This criteria is used in the pass/fail evaluation for each point [33]. Equation 2.1 shows the calculation method:

$$\gamma = \sqrt{\frac{r^2(\vec{r}_{m,}\vec{r}_c)}{\Delta d_m^2} + \frac{\delta^2(\vec{r}_{m,}\vec{r}_c)}{\Delta D_m^2}} \qquad \text{Eq.2.1}$$

where

$$r(\vec{r}_{m,}\vec{r}_c) = |\vec{r}_c - \vec{r}_m|$$

and

Dc is the distance between the calculation data position and test point position

Dm is the distance between measurement data position and test point position

$$\delta\left(\vec{r}_{m,}\vec{r}_c\right) = D_c(\vec{r}_c) - D_m(\vec{r}_m)[33]$$

2.3.2 The Concept Of Dose Correction Factor

In the current dose calculation algorithm, the integral depth dose (IDD_z) is considered to only be related to depth(z cm)[34].Doses delivered to a target after traversing different air gaps (a cm) are all considered to be the same value as when the air gap is equal to 0 cm($IDD_{(z,0)}$). Based on the IDDs acquired by measurements of different air gaps (Figure 2.1B), this assumption is not accurate.

The IDD is dependent upon both depth (z cm) and air gap (a cm).We take the current standard dose calculation $IDD_{(z, 0)}$ and improve it by adding a dose calculation correction factor (G_a) related to the air gap (a cm) to acquire a more accurate $IDD_{(z, a)}$.

$$IDD_{(z, a)} = IDD_{(z,0)} \times (1 - G(z, a)) \tag{1}$$

It is convenient for us to understand how much dose change from current dose calculation method $IDD_{(z,0)}$ to $IDD_{(z,a)}$. $G_{(z,a)}$ stands for the ratio of dose loss related with the air gap (a cm), therefore ($1-G_{(z,a)}$) will be the ratio of dose deposited on the target at the depth z in the target after transporting through the range shifter.

Where:

IDD is the integral depth dose

z is the depth in the water phantom

$G_{(z,a)}$ is the correction factor corresponding to the air gap size (a cm) at depth(z cm)

$G_{(z,a)}$ is calculated using equation (2.2)

$$G_a = \frac{IDD_0 - IDD_a}{IDD_0} \qquad \text{(Eq 2.2)}$$

Where:

IDD_0 is the integral depth dose with air gap a=0 cm (Figure 2.1.A)

IDD_a is the integral depth dose range when an air gap a (cm) exists between range shifter distal surface and water phantom proximal surface (Figure 2.1.A)

$G_{\mathrm{z,a}}$ is the ratio of IDD_a difference to IDD_0

G_{a} for all energies with different air gap (a cm) are calculated for clinical plan simulation.

The main purpose of equipping the range shifter is to take the advantages of the relatively small spot sizes of high-energy beams. In this way, smaller lateral penumbrae can be achieved. When the beam energies are lower than 151.0 MeV the range shifter is rarely used. Therefore, in this study, we only calculate correction factors for proton energies ranging from 151.0 MeV to 228.1 MeV (30 proton energies in total).

2.3.3 IDD Measurements In The Water Phantom

To validate the range shifter simulation model, the dose delivered to the simulated water phantom is compared to the dose delivered to a water tank that is measured using a Bragg peak ion chamber (model 34070, PTW-Freiburg, Freiburg, Germany) (Figure 2.2A). The chamber has a diameter of 81.6 mm and a sensitive volume of 10.5 cm^3. The WET of the chamber entrance window is 4 mm [35, 36] .The range shifter is positioned to create air gaps of 0 cm, 10 cm, 20 cm, and 30 cm for the simulation. The IDDs for 219.3 MeV with 0 cm, 10 cm, and 30 cm air gap, as well as those for 151.0 MeV and 181.3 MeV with a 30 cm air gap, are measured with the water tank [37].

An 82 mm diameter detector is placed in the water phantom of the simulation model (Figure 2.2B) to simulate the IDD curve measured by the Bragg peak chamber. The simulation results are then compared to the measurement results [13].

Integral depth dose (IDD) are applied to compare dose calculation results with the measurement results of the dose delivered to the water tank.

2.3.4 Setup Of Simulations In TOPAS

IDD_0 and IDD_a are acquired by our simulation model. In our previous publication, we built a beam simulation model for the PTCH spot scanning treatment system[38]. The model provides accuracy with multi-energetic field simulations showing errors <5%. The 2% - 2 mm gamma analysis of the clinical plan has a pass rate >97%, while the 3% - 3 mm analysis has a pass rate of 99.9%.

The simulation platform Tool for Particle Simulation (TOPAS) [39, 40] is used to build the beam model. TOPAS (Version 2.0.p3) is a based on the general-purpose Monte Carlo toolkit Geant4 (Version 10.2) [41, 42] , which has been broadly used in proton and particle therapy related research [43-45]. The QGSP_BIC_EMY physics list was selected to provide the accurate dose distribution [46-48]. The parameters of the geometrical model are as displayed in Figure 2.1a. A water phantom with x, y, and z dimensions of 25 cm, 25 cm, and 35 cm, respectively (Figure 2.1A), was built in the simulation. For dose calculations, the voxel has a volume of $1 \times 1 \times 1$ mm^3 in the water phantom [49]. The xy-plane of the water phantom is equal to the field size of the ionization chamber array, MatriXX (IBA Dosimetry, Schwarzenbruck, Germany), which is used in our measurements for patient quality assurance (Refer to section 1.1.6). The z dimension of the water phantom is longer than the range of the maximum beam energy 221.8 MeV. $5\text{x}10^6$ histories were generated per run by the simulations to make the statistical uncertainty < 1%. A double Gaussian beam source model is built for this simulation. The spatial spread of each beam source decreases as beam energy increases. The spatial spread of the first source, $\boldsymbol{\sigma_1}$ **,**was set to range from 5.2 mm to 11.2 mm for beam energies. For energies between

74.5 MeV and 150.0 MeV, the spatial spread of the second source, $\boldsymbol{\sigma_2}$, was set to range from 12.5 mm to 27.2 mm. For energies above 150.0 MeV, the second source was not needed. For energies lower than 80 MeV, the weight for the second source is 0.12. For energies from 80 MeV to 150 MeV, the weight of the second source is 0.08 [39, 50, 51].

The 6.7 cm WET range shifter was modeled between the proton source and the water phantom. The range shifter can be moved in the beam direction to form different air gap distances between the distal surface of the range shifter and the proximal surface of the water phantom. The water phantom proximal surface is fixed at isocenter (Figure 2.1A). Simulation results for all required energies with different range shifter positions are used for correction factor calculation. Two different types of virtual detectors are built in the water phantom (Figure 2.2B). A cylindrical scorer (water) with the radius of 4.08 cm and the thickness of 1 mm is used to model the Bragg peak chamber. Because the spot sizes of low-energy beams are larger than the size of the Bragg peak chamber. A water layer of 25 cm x 25 cm x 1 mm is modeled as the sensitive detector to capture most of the transporting particles. When comparing with the measured IDD, the simulated IDD from the virtual cylindrical detector is used. When calculating dose correction factors, the simulated IDD from the large virtual cubic detector is used. The number of particles (primary protons and other secondary particles) arriving at the entrance plane of the water phantom is also scored.

2.3.5 Correction Factor Validated By Clinical Plan

To validate the accuracy of the correction factor, a clinical head and neck treatment field was simulated and the correction factor $G_{(z,a)}$ is applied to the dose calculated by the standard algorithm using Equation (2.1).

In our dose calculation algorithm for treatment plans not using the range shifter, the simulation dose (Gy/history) is converted to real dose (Gy/MU) by following equation (2.3).

$$Dose_{real} = \frac{IDD_{Measurment}}{IDD_{simulation}} \times Dose_{\text{simulation}} \qquad \text{(Eq 2.3)}$$

The improved dose calculation equation applied to the treatment plan calculation will be:

$$Dose_{real} = \frac{IDD_{Measurment}}{IDD_{simulation}} \times (1 - G_{\text{z,a}}) \times Dose_{\text{simulation}} \qquad \text{(Eq 2.4)}$$

$Dose_{real}$ is the dose at specific point at depth z cm.

$IDD_{Measurment}$ is the configuration integral depth dose per MU(monitor unit) for proton energy E MeV

$IDD_{simulation}$ is the simulation integral depth dose Gy/history for proton energy E MeV

$G_{\text{z,a}}$ is the correction factor for depth z cm and air gap a cm

$(1 - G_{\text{z,a}})$ is applied in equation (2.4) to correct the $IDD_{Measurment}$ from air gap 0 cm to air gap a cm.

The result is compared to the patient-specific quality assurance measurements of that were performed by a clinician for this plan. The treatment field gantry angle was 300̊, with an energy range of 98.0 MeV to 173.7 MeV. The field has 1821 scanned spots. The measurement data for this plan was acquired using a solid water phantom with a MatriXX 2-dimensional ion chamber array. For each beam, 250,000 events were generated. Gamma test is performed using 3% - 3 mm evaluation criteria. To accomplish this, the 7.2mm × 7.2mm grid is bilinearily interpolated to a 1 mm × 1 mm grid. The threshold level of the dose for the gamma analysis was set to 10% of the maximum dose.

2.4 Result

2.4.1 Simulation Results Validated By IDD Measurements In The Water Tank

The measurement data of 219.3 MeV is compared with the simulation data from the detector in the model simulation results (30 cm and 10 cm) (Figure 2.3.A&B), yielding a mean difference of 0.9% and 1.0%, standard deviation are 0.9% and 0.9%. Measurement data of 151.0 MeV (Figure 2.3C) and 181.1MeV, both with air gaps of 30 cm (Figure 2.3D) are compared with simulation data. The mean differences are 1.3% and 1.2%, standard deviation are 1.1%and 0.5%, respectively.

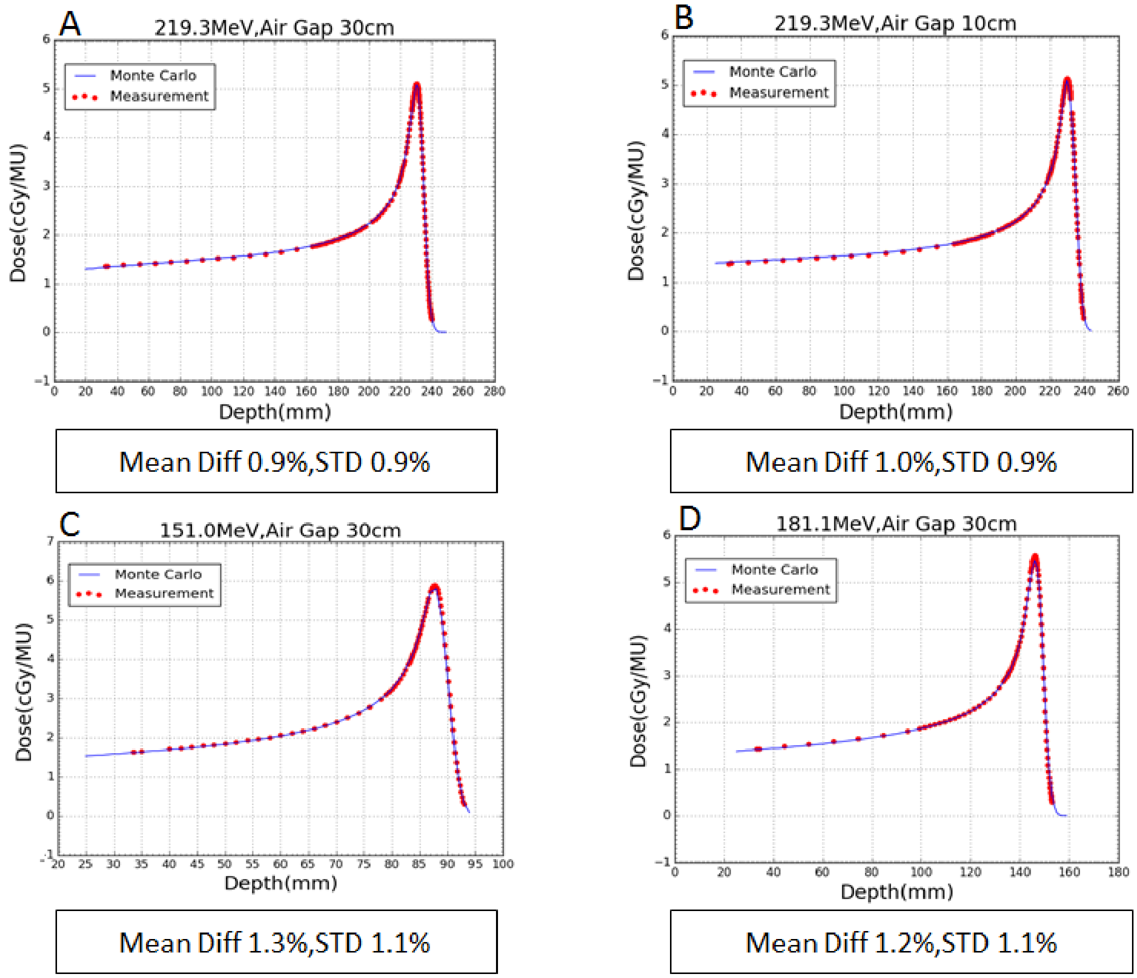

Figure 2.3 Comparisons of IDD distributions between simulations (solid lines) and measurements (red dots) for different proton energies with different air gaps. MU stands for monitor unit. Simulation results are from the virtual cylindrical detector with the same dimension of the Bragg peak chamber used in the IDD measurements.

2.4.2 The Simulation Results From Large Scorers

We also performed the simulations with large scorers (25 cm x 25 cm x 0.1 cm) to score IDDs and the acquired data are used to calculate the dose correction factors at different depths for different air gaps. The simulation results for 221.8 MeV protons with different air gaps are compared in Figure 2.4. It demonstrated that with the increase of air gap distance, the dose from entrance plane to plateau region is decreased. This is due to the lateral scattering of beam passing through the range shifter. Since the distance between source plane and the entrance plane of the range shifter is very long (Figure 2.1A), we can assume the scattering angle of beam exiting the range shifter is not affected by the distance between source plane and the entrance plane of the range shifter. After passing through the range shifter, the scattered beam will travel in the air gap and then enter the water phantom. Obviously, a longer air gap distance will cause a larger lateral spread of beam spot, which may result in the loss of particles arriving at the entrance plane of the water phantom. We have investigated the number of different particles (primary protons and all other secondary particles) arriving at the entrance plane of the water phantom. The number of primary protons and the number of secondary particles are listed in Table 2.1. Our data show that the number of primary protons decreases slightly with the increase of air gap, but the number of secondary particles can be largely affected by the air gap. More secondary particles are scattered laterally away from the central axis and may not enter the phantom, resulting in a decrease of energy deposition in the scorer (25 cm x 25 cm x 0.1 cm). This turns into the decrease of total dose as shown in Figure 2.4. The simulated dose data are then used to calculate the dose correction factors.

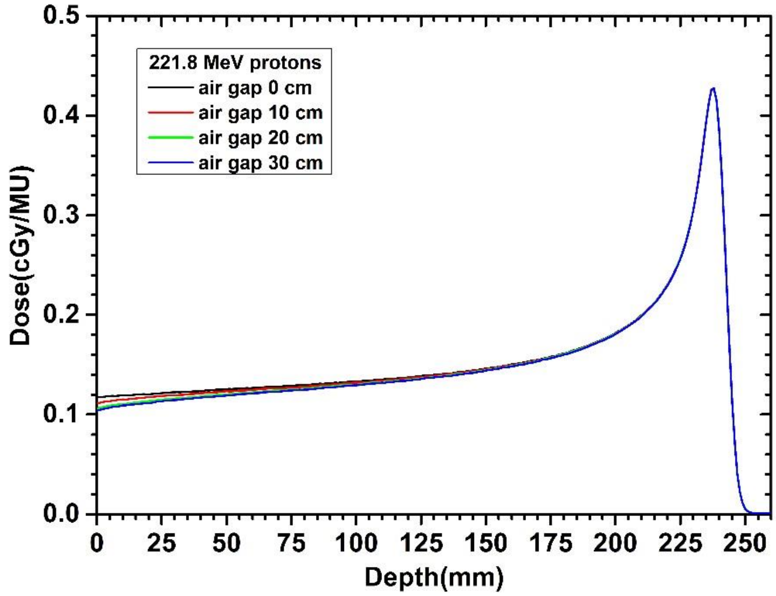

Figure 2.4 The IDD distributions of 221.8 MeV protons with different air gaps. In the Monte Carlo simulations, the dimension of the soccer is 25 cm x 25 cm x 0.1 cm. A larger air gap can result in a lower dose from the entrance to the plateau region.

Table 2.1 The number of particles at the entrance plane of the water phantom with different air gaps. The initial number of source protons is 10^6.

Air gap	0 cm	10 cm	20 cm	30 cm
Number of primary protons	935164	933866	930547	929027
Number of secondary particles	213349	127951	84720	64867

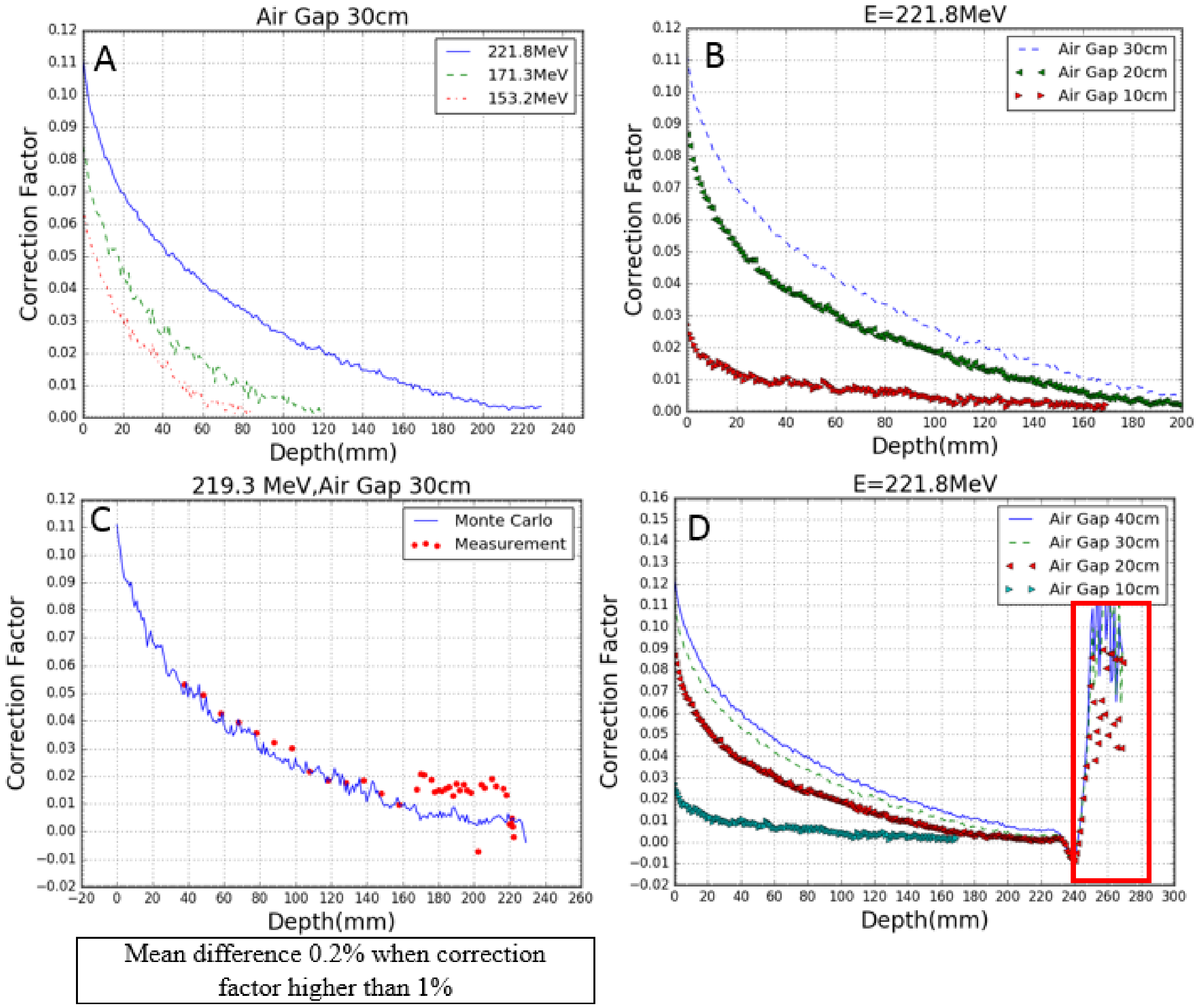

Figure 2.5 Simulation results (A) Correction factor depth profile for proton energy 221.8 MeV, 171.3 MeV and 153.2 MeV with air gap 30 cm (B) Correction factor depth profile for proton energy 221.8 MeV with air gap 10 cm, 20 cm, 30 cm (C) Correction factor validation by measurement result (D) Correction factor effective range for proton energy 221.8 MeV.

With a constant air gap, the correction factor decreases as energy decreases. The largest correction factor is 0.11 for proton energy 221.8 MeV at depth 0 cm and air gap 30 cm (the highest air gap that can be measured for our system) (Figure 2.5A).

With a constant air gap and energy, the correction factor decreases as depth increases (Figure 2.5B).The correction factors are only calculated for proton energies from 150 MeV to 228.1 MeV (30 proton energies in total) for this paper because the correction factor of energies lower than 150 MeV are too small (<0.01 for energies with ranges <2 cm) to count in the dose calculation (less than 0.01 after depth 2 cm).

Correction factor of 219.3 MeV measurement and calculation maximum difference is 0.7% when the correction factor is higher than 1.0%. Because the accuracy requirement for clinical application is the dose deviation shall be within 3%, the result would satisfy our clinical requirement (Figure 2.5C).

The correction factor for each proton energy is a random number at depth after Bragg peak presents (Figure 2.5D) which means the effective range of the correction factor is from target surface to the Bragg peak depth in the target.

2.4.3 Proton Fluence Simulation Results From Scorers

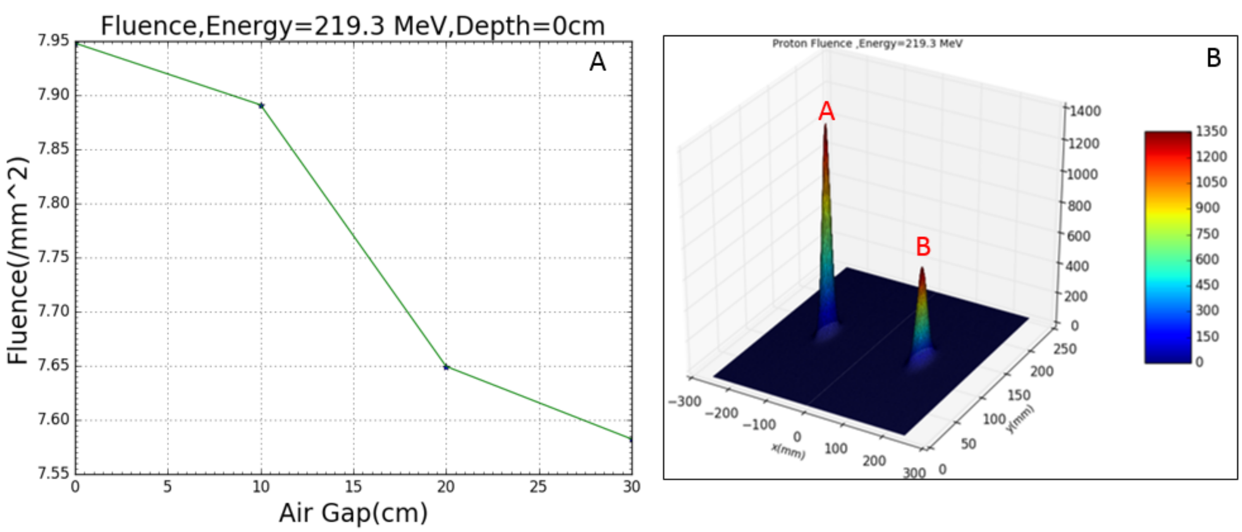

Figure 2.6 (A) Fluence of water phantom surface vs range shifter position (air gap) (B) Peak A is fluence of the water phantom surface when air gap equals to 0 cm， peak B is fluence when air gap equals 30 cm

For energy 219.3 MeV, at the water phantom surface (Depth=0 cm), 500,000 proton partials histories were generated by the simulations. The proton fluence decreased from 7.95 /mm^2 to

7.582 /mm^2 as the air gap increased from 0 cm to 30 cm (Figure 2.6A). The range shifter prevents some of the protons from reaching the water phantom, as some are lost in the air gap. This is due to the beams being scattered after passing through the range shifter .That is why the dose, calculated at corresponding test points downstream from the range shifter, decreases as the air gap increases. (Figure 2.5B).

From Figure 2.6B we find that the fluence distribution of peak A, with an air gap of 0 cm, is different than that of peak B, which has an air gap of 30 cm. The blue part of peak A is much smaller than the blue part of peak B which means that the low fluence area in A is much smaller than that region in B. When the air gap is greater, the protons spread in a larger area. Peak A is much higher than peak B which also supports that when the air gap is smaller, the protons distribute in a more narrow area.

2.4.4 Correction Factor Validated By Clinical Treatment Plans

The calculation from the TPS (Eclipse Versions 8.917, Varian Medical Systems, Palo Alto, CA,USA) resulted in a gamma result that was lower than our clinical requirement (gamma pass rate of 90% using 3% - 3 mm evaluation criteria). After applying the correction factor, the gamma pass rate increased from 80.4% to 97.8%. Because the high proton energies are shifted by the range shifter in the clinical plan, a correction factor was used on the dose calculation result. Figure 2.7 shows that for the a field at a depth of 11.9 cm, and using evaluation criteria of 3% - 3 mm the gamma pass rate increased from 80.4% to 97.8%.

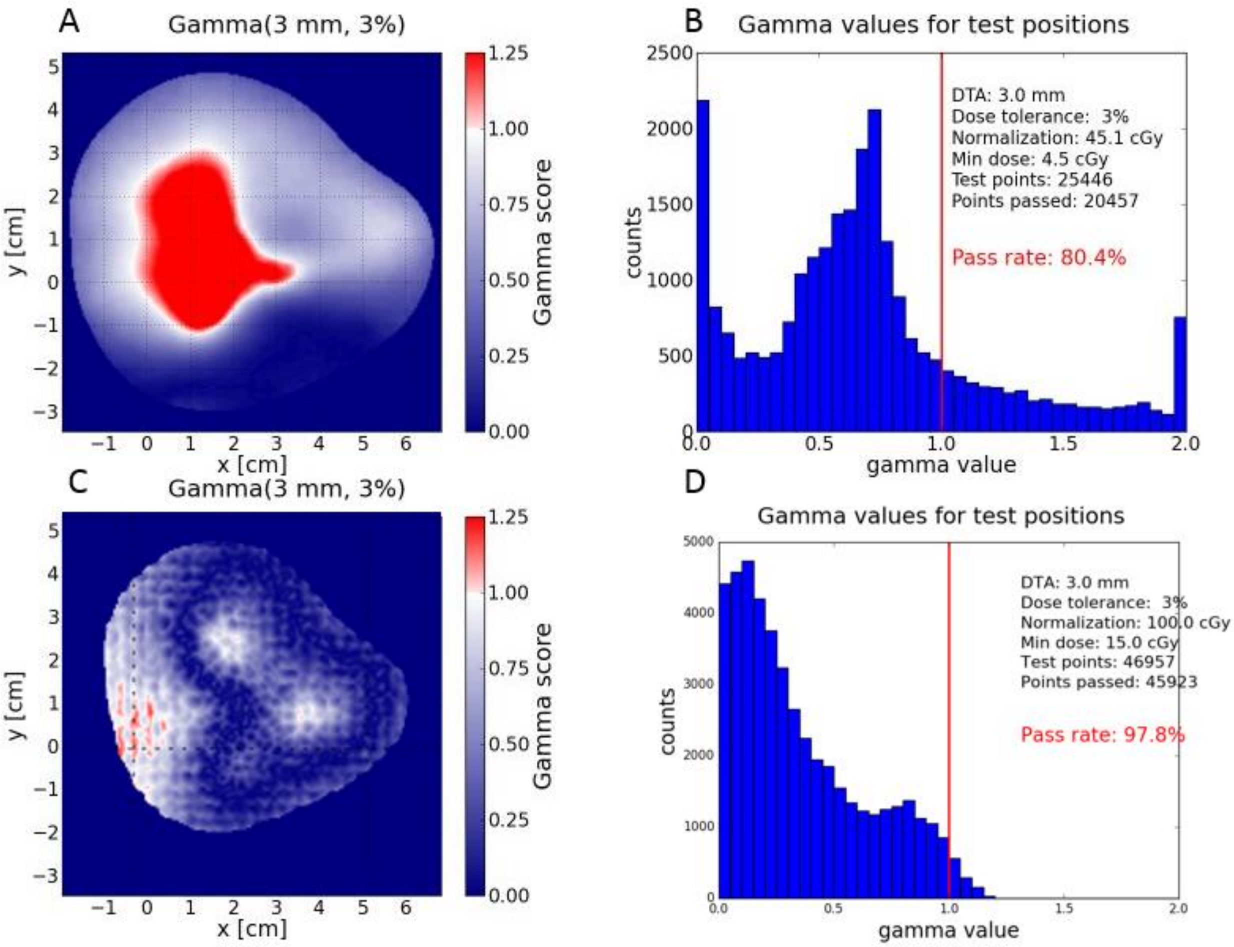

Figure 2.7 Measurement compared with TPS and measurement compared with simulation applied correction factor at depth 11.9 cm using gamma analysis. (A) TPS compared with measurement result using gamma analysis. (B) Gamma pass rate histogram of TPS vs. measurement (C) Simulation with correction factor compared with measurement result using gamma analysis. (D) Pass rate histogram of simulation with correction factor vs. measurement

Only energies higher than 166.2 MeV could deliver dose to a depth of 11.9 cm after traversing the 6.7 cm WET range shifter, a total depth of 18.6 cm WET. According to the effective range of the correction factor (Figure 2.5D), the correction factor applies to energies higher than 166.2 MeV in the treatment plan. (Table 2.2).

Table 2.2 Correction Factor for Air Gap a=30.0 cm, depth=11.9 cm

Proton Energy(MeV)	Factor(Ga)
173.7	0.0110
171.3	0.0050
168.8	0.0021
166.2	0.0014

The other cases are tested for the correction factor, the pass rate improved from 80.0% to 99.8% at depth 5.0 cm for a head and neck plan. The pass rate improved from 87% to 93.7% for a Thorax plan (Table 2.3).

Table 2.3 Comparisons of Gamma pass rate for a thorax plan and a head&neck plan before and after applying correction factors.

Case Type	Air Gap(cm)	Depth(cm)	Gamma Pass Rate (%)	
			Before	After
Head neck	30	5	80	99.8
Thorax	20	3.7	87	93.7

2.5 Discussion

According to the results of Table 2.3, the dose calculation accuracy improved by the correction factor well mostly on distal and proximal of the target. This is because only high energy protons can deliver dose to the distal part of the target and the high energy proton all need to apply correction factors. At proximal part, even the dose weight from high energies proton is low, but the correction factor is bigger than in distal part (more than 3% dose difference).The quality assurance for treatment plan fail mostly occurs at distal and proximal because the analytical model in treatment planning system didn’t count the fluence lost. This correction factor data set shall be added to any calculation related with this type of range shifter.

It is difficult to acquire continuous correction factor data from measurement because the labor and beam cost are very high. The range shifter model could be used to do patient-specific dose calculations, but it would be as slow as the common Monte Carlo method. The majority of TPSs still use analytical dose calculation algorithms for optimization and final dose calculation. TOPAS simulation could help to improve the dose calculation algorithm by modeling the experimentally challenging configurations. Preparing a correction factor data set by this range shifter model simulation is, perhaps, the most practical way to improve the accuracy of current dose calculation engines. Applying the factors to specific proton energies based on the air gap, dose verification simulation accuracy could be improved without heavily modifying the current system.

2.6 Conclusion

We found that proton fluence was being lost in the air gap in our clinical practice, which led to a reduction of dose to the target. We propose to build a correction factor data set to improve the accuracy of current range shifter modeling for dose calculation of proton treatment analysis system. The calculation results match the measurement results acquired using a Bragg peak ion chamber in a water tank. By incorporating the correction factors into the current dose calculation method, the dose calculation accuracy of patient treatment fields using a range shifter can be significantly increased. The correction factor data set could be generated in our range shifter model and applied for future dose calculation. This method could likely be applied to our proton treatment analysis system in a flexible way.

3 An Automated Quality Management Of Spot Cluster Algorithm As A Safety Procedure For Implementing Pencil-Beam Scanning Proton Therapy

3.1 Abstract

Purpose: To develop an automated quality management to detect the potential error in the proton spot scanning delivery process based on knowledge extraction of the previous delivered fields.

Methods: 1297 treatment fields from 2014-2016 in our center were analyzed for the knowledge extraction. Proton spot distributions are transferred to binary matrix. A connected-component labeling algorithm is developed to label all the spot clusters.

Result: The threshold for small spots clusters is established with algorithm analysis. Once the field is identified as the small spots cluster that is less than the threshold, an alert will be automatically sent out to prevent the potential accident or other mistakes by the filters developed in house in our center. Three types of error will be automatically detected by the proposed algorithm: 1) the contouring error for the targets; 2) the unnecessary small cluster at the distal end causing the dose distribution not passing the quality assurance (QA) criteria; and3) Abnormal high dose region outside target.

Conclusion: The automated quality assurance procedure based on data mining of the previous delivered fields can prevent the errors and improve the quality assurance process for the proton spot scanning delivery.

3.2 Introduction

The narrow proton beam used in active beam delivery in proton treatment defines as spots. Spots are scanned laterally by magnetic steering in the plane perpendicular to the beam direction, creating a large field free from scattering elements such as aperture or compensation [52, 53] . Monoenergetic spots with different energies form a synchrotron that can be stacked to deliver the specified dose distribution along the direction of the beam. It is possible to modulate the intensity of each spot in order to deliver a conformal three-dimensional (3-D) dose to the target volume [6, 54-57]. 3-D dose distributions are built in a discrete fashion by delivering the dose spot-by-spot and energy “layer-by-layer” [35, 36]. Thus, an individual spot acts as the building block for the creation of 3-D dose distributions [58]. In addition, the spot distribution map may provide information that helps detect errors in treatment plans.

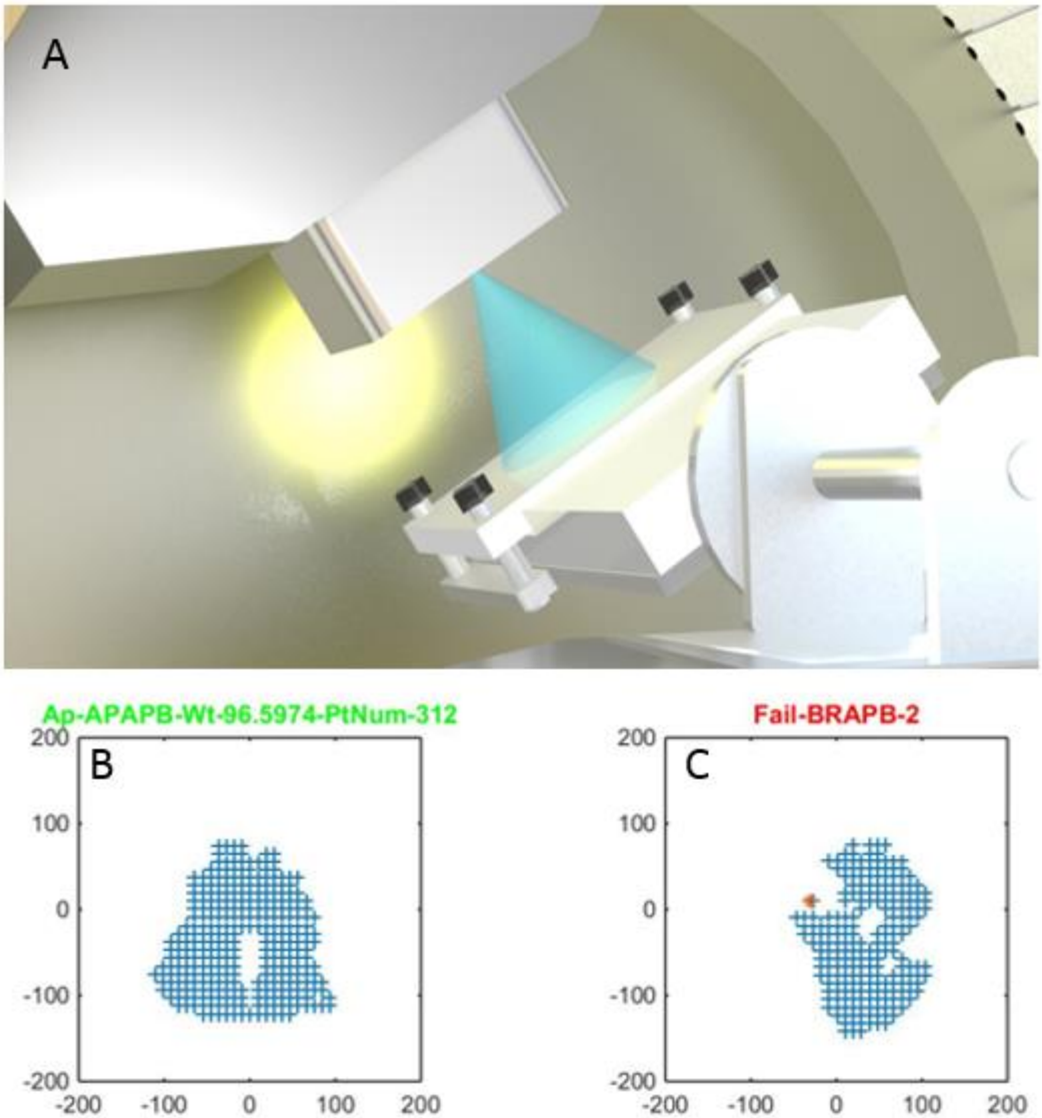

Figure 3.1 Scanning Spot Nozzle and the spots pattern.(A)Scanning spot Nozzle(B)Spots cluster pattern.(C)Small spot cluster(Red spots)

In our clinical practice, we define groups of spots constituting of the projection of proton spots position on x-y plane as clusters (Figure 3.1B).Some of clusters with small spots amounts are usually hard to see with the naked eye. However, small clusters sometimes signify a high dosage area which must be managed (Figure 3.1C). Now we will discuss an algorithm used in the analysis of clusters. A tool based on this algorithm could provide a warning for physicists and dosimetrists to notice these small clusters and optimize treatment plans.

3.3 Method And Material:

From 2014-2016, there were 1,241 treatment plans delivered to patients in PTCH. The plans were used to acquire the minimum number of spots within clusters for each treatment site. Normally if the number of spots in one cluster is smaller than the minimum number designated in a treatment plan, the cluster is considered as a small spot cluster and will be highlighted within the treatment plan. Forty different treatment plans, each having been revised during the treatment process, have been used to validate a small spot cluster analysis algorithm.

3.3.1 Transfer Spots Distribution Maps To Matrices

The spots distribution maps are drawn from the dicom files exported by the treatment planning system (Figure 3.2A). The proton spots distribution position in millimeters on x-y plane are changed to Matrix x-y coordinate (Figure 3.2B). All numbers are rounded to integer coordinate. The corresponding position in matrix are labeled as 1s and the other coordinate are labeled as 0s.The spots distribution is changed into binarization matrix at this step. The 1s in Matrix are components used in next step for connected-component labeling algorithm (Figure 3.2C)

A

x(mm)	y(mm)
3	4
4	3
4	4
8	6
8	7
7	7
2	8
2	9
3	8
3	9

B

	1	2	3	4	5	6	7	8	9
1	0	0	0	0	0	0	0	0	0
2	0	0	0	0	0	0	0	1	1
3	0	0	0	1	0	0	0	1	1
4	0	0	1	1	0	0	0	0	0
5	0	0	0	1	0	0	0	0	0
6	0	0	0	0	0	0	0	0	0
7	0	0	0	0	0	0	1	0	0
8	0	0	0	0	0	1	1	0	0
9	0	0	0	0	0	0	0	0	0

C

	1	2	3	4	5	6	7	8	9
1	0	0	0	0	0	0	0	0	0
2	0	0	0	0	0	0	0	3	3
3	0	0	0	1	0	0	0	3	3
4	0	0	1	1	0	0	0	0	0
5	0	0	0	1	0	0	0	0	0
6	0	0	0	0	0	0	0	0	0
7	0	0	0	0	0	0	2	0	0
8	0	0	0	0	0	2	2	0	0
9	0	0	0	0	0	0	0	0	0

Figure 3.2 Transfer spots distribution map to matrices. A Coordinate list of spots position, B Binary matrix acquired by the spots distribution map, C label clusters by connected-component labeling algorithm

3.3.2 Connected-component Labeling Algorithm[59]

The connected-component labeling algorithm is usually applied to locate objects for visual applications. The labeling algorithm categorizes the binarization matrix into different groups using the connectivity of component neighboring the processed component. The connected-component labeling algorithm searches for and labels possible candidates by dividing foreground components into groups using their eight-connectivity relationship. Components which connect in horizontal, vertical and diagonal directions are considered as one group (Figure 3.3A). Once the background subtraction algorithm has segmented all groups from the background of the spots plane, the connected-component labeling algorithm begins its process of locating groups. The labeling algorithm collects and merges components into groups by judging the eight-connectivity of the foreground components and adjacent neighboring components (Figure 3.3B). Subsequent the application of the labeling algorithm, the location, size, and number of foreground groups are ascertained, which helps to determine candidates for group detection .Connected-component labeling algorithm is processed by Matlab R2014a imaging processing toolbox.

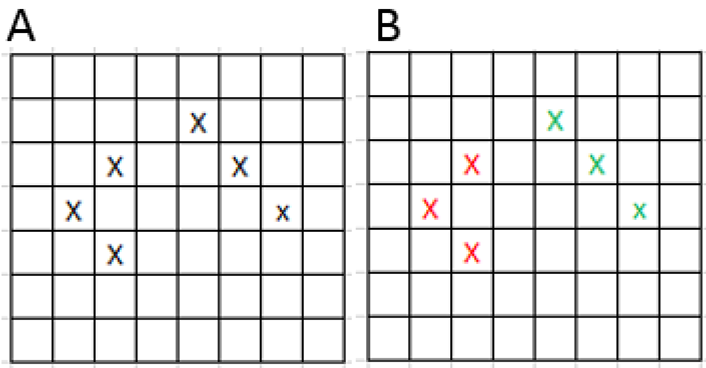

Figure 3.3 (A) 1 group under 8-connection area include connected area in diagonal criteria (B) 2 clusters under 8-connected-componets criteria, red group and green group

3.3.3 Small Spots Clusters Labeled By Connected-component Labeling algorithm

The matrices generated by spots distribution map are labeled by connected-component labeling algorithm (Figure 3.2C). The number and size of groups of each treatment plan are recorded for analysis.

3.4 Results

3.4.1 Minim Spots Number Of Delivered Treatment Plans

Table 3.1 Minim spots number of delivered fields

		Number of Spots		
	Num of Case	Mean	Max	Min
Head& Neck	465	465	816	6
4D throx	108	137	522	23
Throx	90	124	373	11
Prostate	107	208	433	45
Brain	119	50	128	7
PELVIS	6	204	456	28
CSI	6	45	94	15
Other	396		756	5

Table 3.1 last column shows minim spots number of treatment plans for each treatment site. These numbers will be used as threshold for small spots clusters detection. The clusters with a

spot number less than the minim number of corresponded treatment site is considered as small spots clusters.

3.4.2 Statistical Relationship Between Small Spots Clusters And Errors In Proton Treatment Plans

Of the 1,294 treatment plans tested by small spot cluster analysis, (53) contained more than a single cluster (Figure 3.4). All (40) treatment plans that had been revised during the treatment process had small spot clusters (Table 3.2 Revision column). Out of the (40) revised plans, (26) failed in our quality assurance process (Table 3.2 QA Fail). Quality assurance concerning an effective, individualized protocol during spot scanning proton treatment has been introduced in other research reports [12, 60]. Overall processing time for the 1,294 treatment plans took one hour, with time spent on each plan averaging 2.7 seconds.

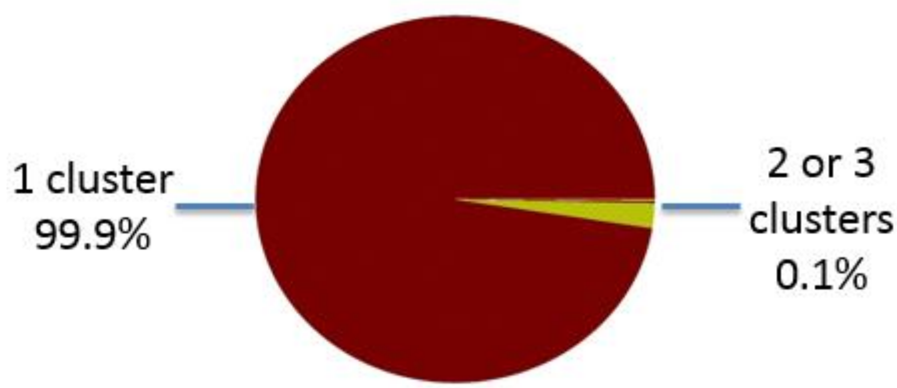

Figure 3.4 Pie Chart of clusters amount of the treatment plans

	Num of Case	Report	Revision	QA Fail	Revision Rate (%)
Head&Neck	465	21	16	10	100%
4D throx	108	6	1	3	66%
Throx	90	3	1	2	100%
Prostate	107	0	0	0	N/A
Brain	119	0	0	0	N/A
PELVIS	6	0	0	0	N/A
CSI	6	0	0	0	N/A
Other	396	10	5	11	100%

Table 3.2 Small spots clusters test result

3.5 Discussion

Based on the results in Table 3.2, small spots clusters analysis algorithm is sensitive to three types of error in proton treatment plans.

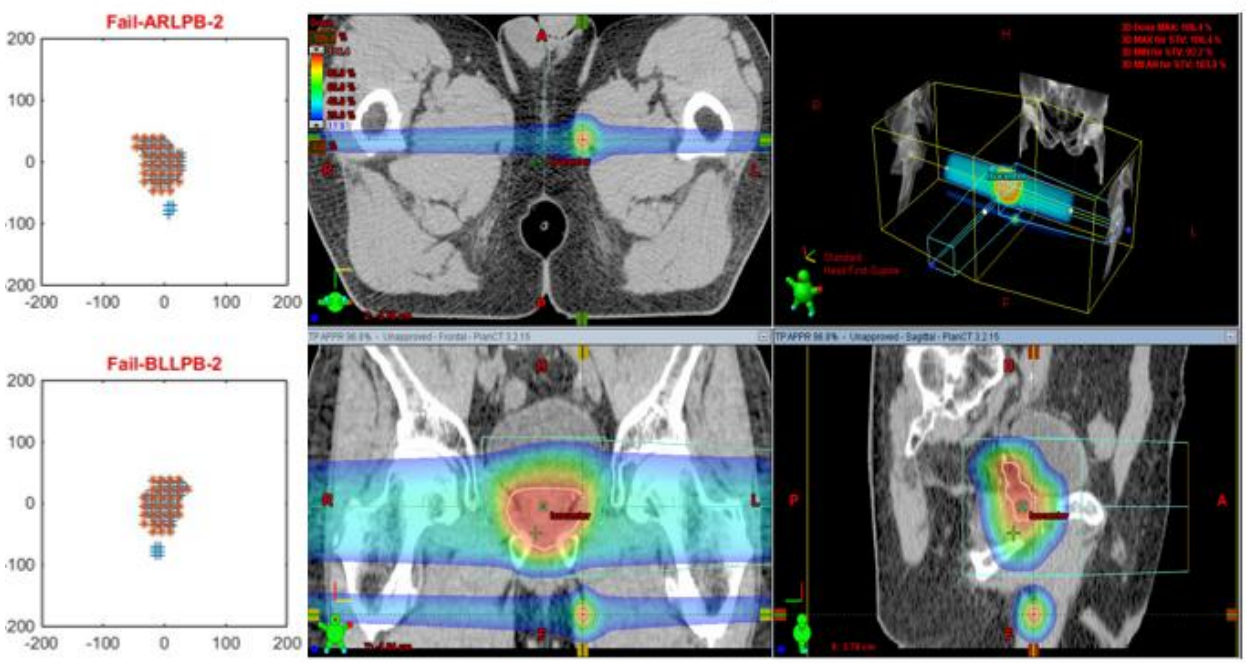

Figure 3.5 Mistake contouring detected by small spots clusters analysis, the blue clusters in the left clusters map are the mistake contouring spots clusters

The first type of error is target contoured by mistake. This type of error would be hard to check manually. The small spots clusters analysis algorithm is able to detect this type of error in the treatment plans (Figure 3.5）.The dosage points, which is created by faulty contouring, corresponds to the small spots clusters (blue) in the cluster map. The small spot clusters contain less spots than the minim spots number inside clusters of correct treatment plans (Treatment plans have already been approved by oncologist). Since this type of error often goes unnoticed, the algorithm could prevent such mistakes and help correct them. All treatment plans with this type of error are detected by the algorithm.

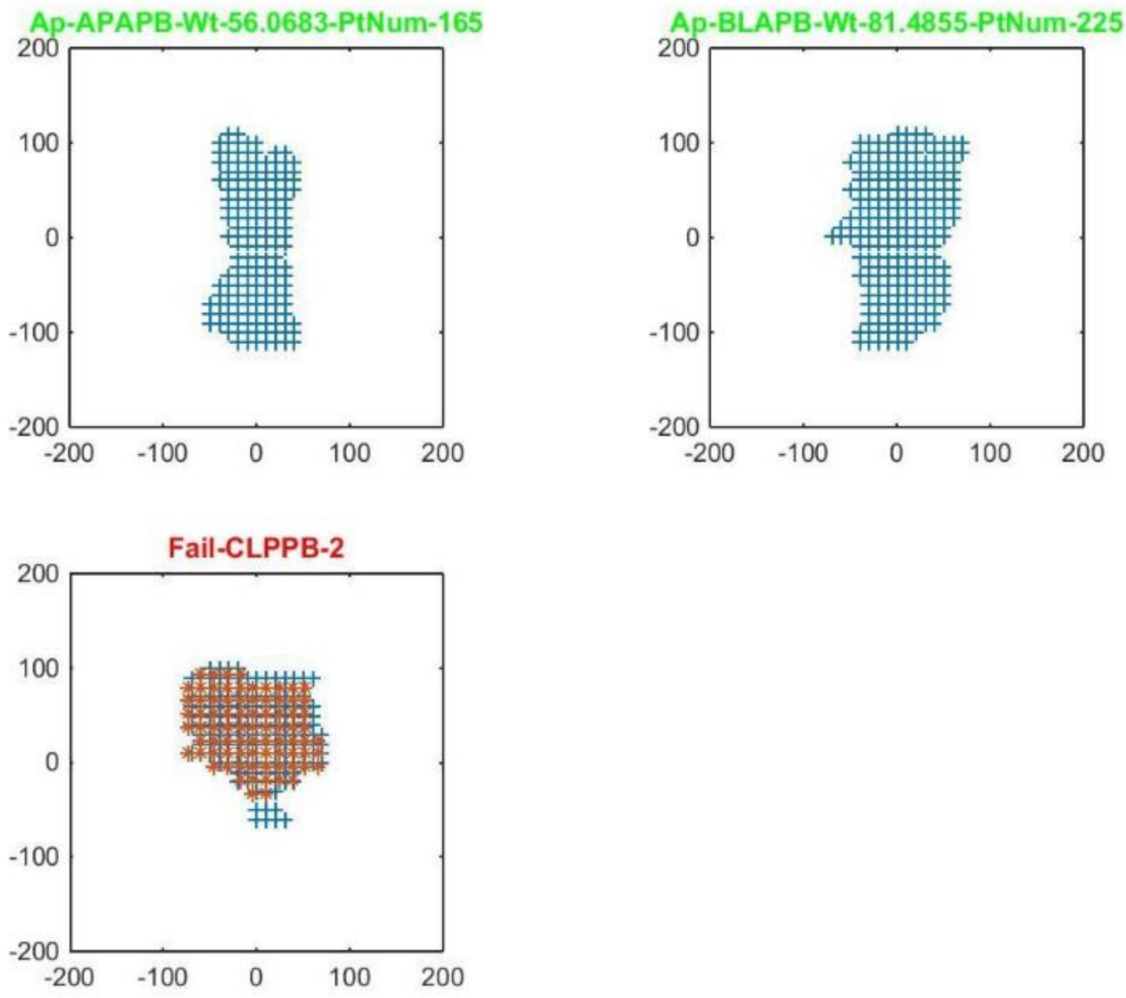

Figure 3.6 Treatment plans with unnecessary spots at distal end of the beam by the small spots clusters analysis algorithm

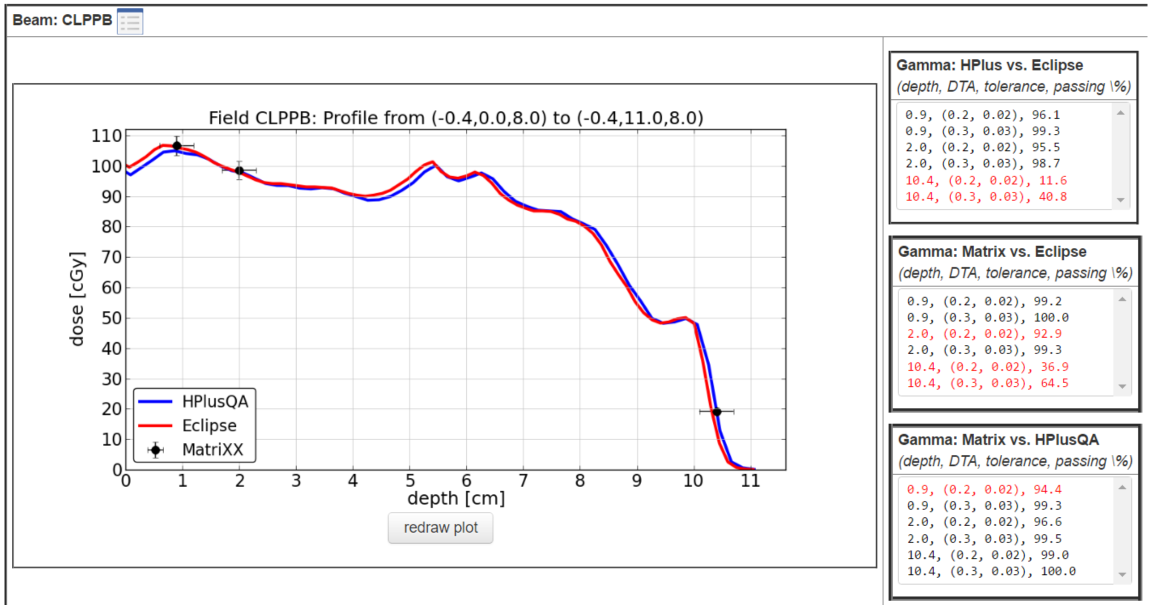

Figure 3.7A treatment plan with small spots cluster fail in quality assurance at distal end of beam

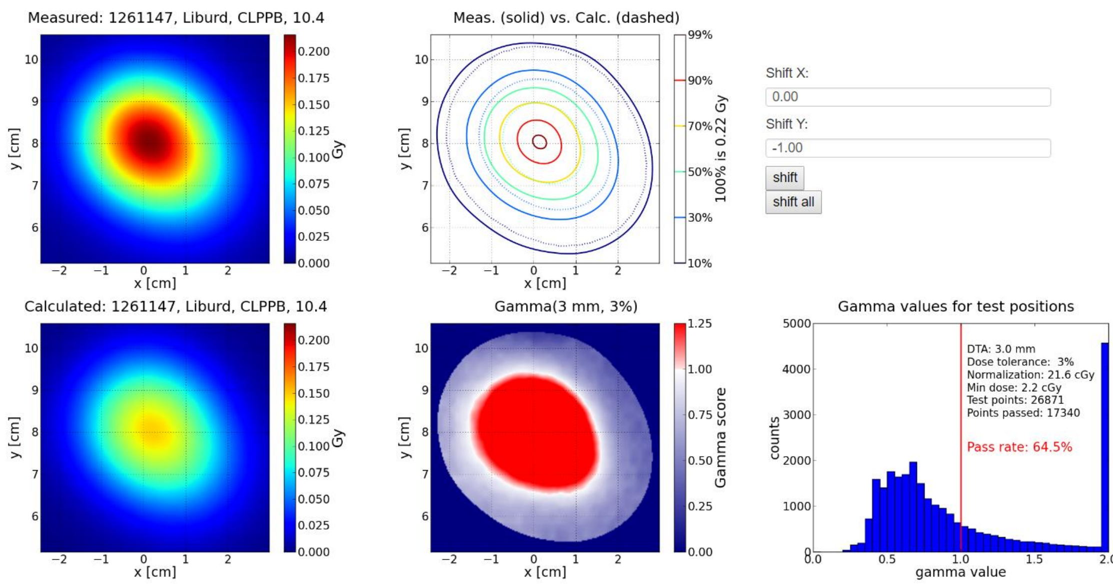

Figure 3.8 Dose distribution map of Treatment plan failed in quality assurance detected by small cluster analysis algorithm

A second problem could be detected by small spots cluster analysis algorithm is that the treatment plans with distal points cannot pass the quality assurance process (Figure 3.6). Please refer to our previous research report regarding quality assurance processes [60]. All of the reported treatment plans that cannot pass quality assurance are led by distal points in the direction of the beam. Calculated results by TPS do not match the measurement results (Figures 3.7&3.8).The dose distribution in a high dosage area at a distal plane is of significant difference compared to the measurement data (less than 70% of test points could pass the gamma test). For this reason, it is a good idea to discuss this topic in the future. At the moment, a decent alert system remains in place for medical physicists to optimize treatment plans.

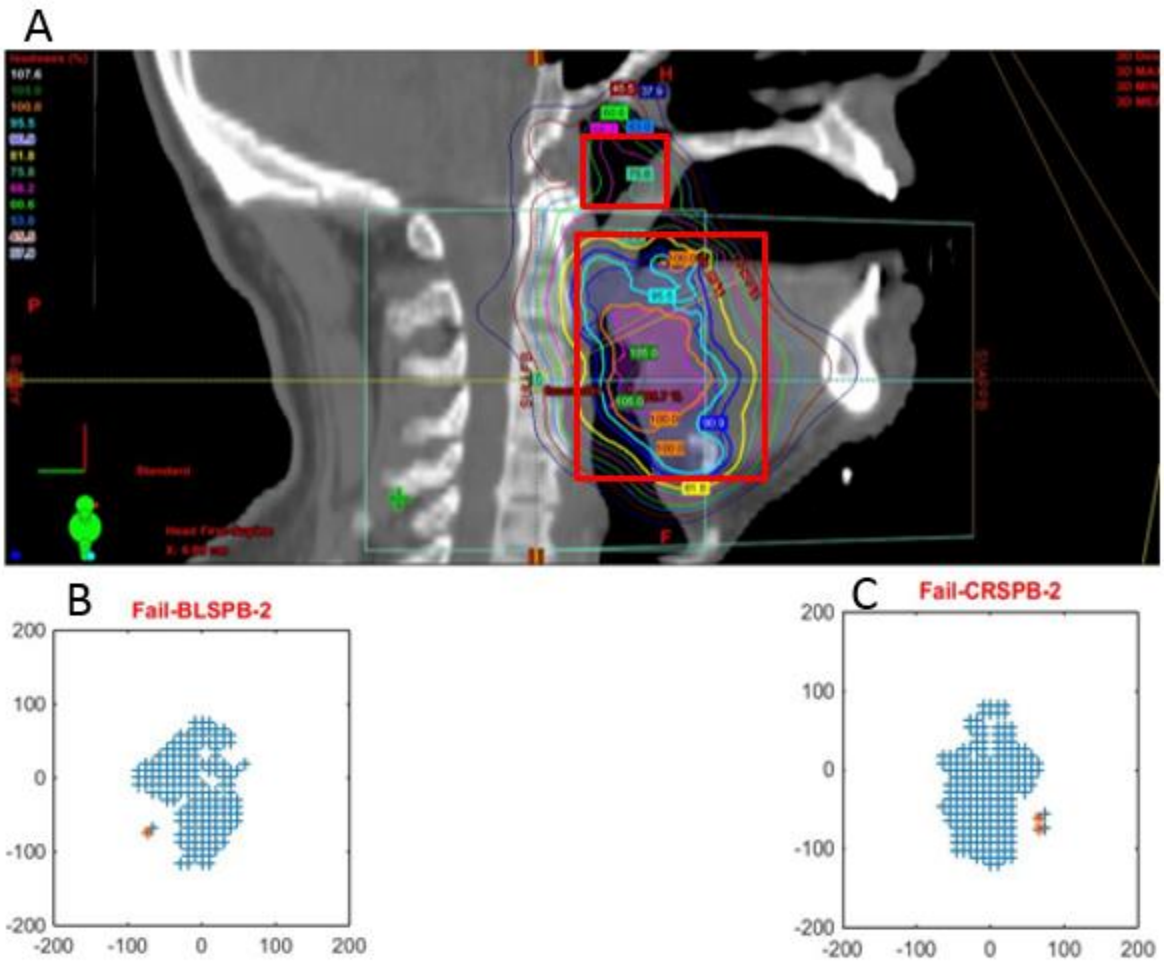

Figure 3.9 Small clusters corresponding to two hot areas inside the target volume (A). The two hot areas are outlined with red squares (B). A small spot cluster is marked by points corresponding to the left side of figure A (B). A small spot cluster is marked by points corresponding to the right side of figure A

The third type of error is that there are two hot areas inside the target volume (Figure 3.9). These types of plans are usually optimized, since treatment plans with two targets are hard to control. This is a good reference for the medical physicist.

For treatment plans concerning the head and neck, 4D Thoracic and Thoracic, only one 1 out of 30 treatment plans with small spots clusters were not revised. This proves that the small spot cluster analysis algorithm is very effective for detecting error in these types of treatment plans.

No revised treatment plans were detected concerning the prostate, brain, pelvis, and CSI. The algorithm is not as sensitive in detecting errors for these types of treatment plans.

3.6 Conclusion

The small spots cluster analysis algorithm could detect errors such as failure of quality assurance and mistake contouring in treatment plans at a very low cost. Use of this tool can improve the efficiency of proton treatment analysis system could reduce the cost of treatment. As a result, its potential for future use in a clinical setting is promising.

4 Fast Dose Calculation By Matrix Registration Algorithm

4.1 Introduction

Proton therapy is becoming an increasingly valuable radiotherapy option for use around the world[61]. Through this method, protons are applied to irradiate tumors. Proton therapy can significantly reduce dose distribution to organs at risk (OARs), located distally from the tumor, while maintaining or even increasing the prescribed dose to the tumor directly. Accuracy can be compared with Intensity Modulated Radiation Therapy (IMRT), which uses x-rays[62],[63]. The advantage of proton therapy is based on the fact that protons stop at a certain, energy-dependent depth, a point recognized as the Bragg Peak[64] where they will deliver most of their energy.

The absolute dosage must be calculated via a dose calculation program according to the energies, spot positions, and number of monitor units (MUs) in order to protect healthy tissue and to deliver the correct dosage to the tumor. The current dose calculation program, based on the TOPAS simulation tool, may take as long as 5 hours to retrieve a dose calculation for an individual patient [50]. Hence, the treatment available at our center is dependent upon a significant amount of time.

The aim of this study is to build a fast dose calculation tool, based on the matrix registration algorithm. This method has been evaluated by measurement data collected at the MD Anderson Proton Therapy Center.

4.2 Material And Method:

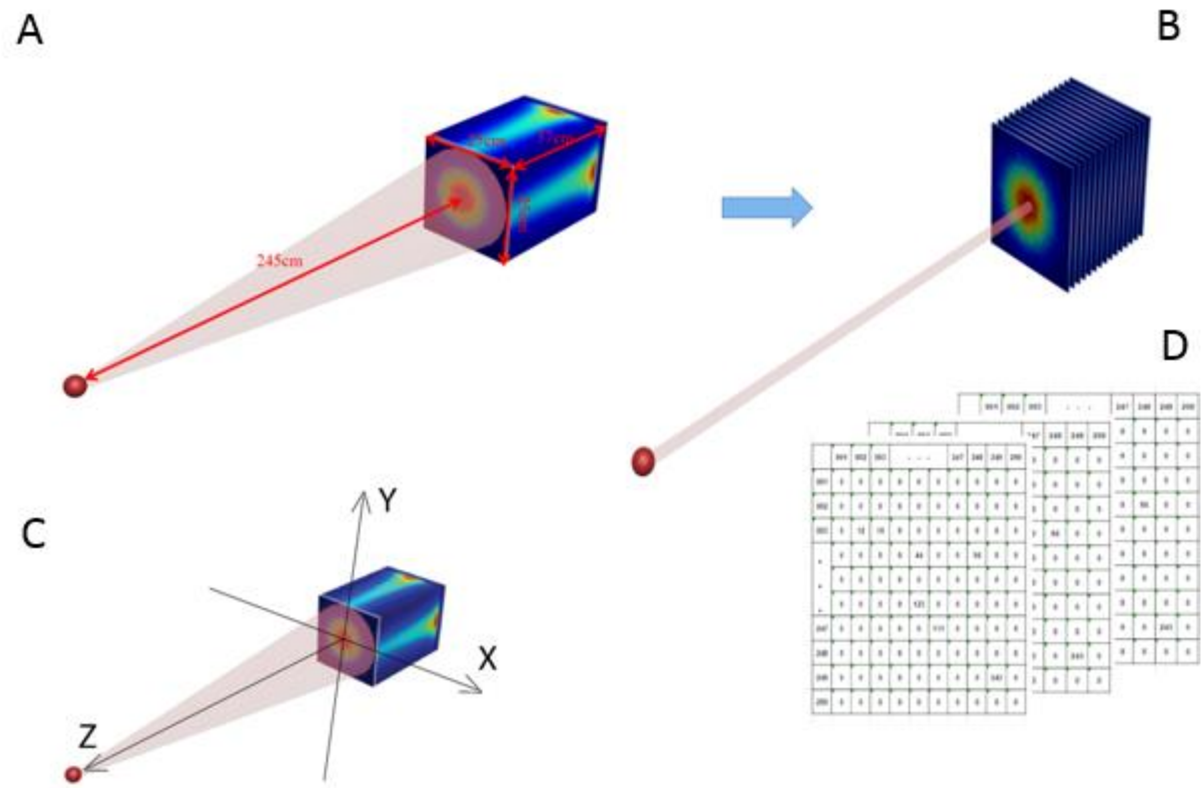

Figure 4.1 Fast dose calculation process. A simulation model in TOPAS.B. Pre-stored dose distribution matrices. C. Coordinate direction of the simulation model

4.2.1 General Working Process Of Fast Dose Calculation Method

1. A simulation model is built using the TOPAS simulation tool, based on the parameter in Figure 4.1A.

2. The dose deposited to the water phantom for all proton energies (94 total) is calculated by the simulation model using TOPAS and stored in sliced images as seen in the dose distribution matrices (Figure 4.1B&D).

3. Dose distribution matrices of individual energy will be loaded and added together to reconstruct a new dose distribution matrix (Figure 4.2).

4.2.2 Simulation Model Of Individual Energy By TOPAS

TOPAS simulation tool is introduced in Chapter 1(Section 1.1.5).Simulation model is set as following parameters. The QGSP_BIC_EMY physics list was selected to provide the accurate dose distribution [46-48]. The parameters of the geometrical model are as displayed in Figure 4.1A. A water phantom with x, y, and z dimensions of 25 cm, 25 cm, and 35 cm was built in the simulation. For dose calculations, the voxel has a volume of $1 \times 1 \times 1$ mm^3 in the water phantom [49].A double Gaussian beam source model is built for this simulation. The spatial spread of each beam source decreases as beam energy increases. The spatial spread of the first source, σ_1, *was* set to range from 5.2 mm to 11.2 mm for beam energies. For energies between 74.5 MeV and 150.0 MeV, the spatial spread of the second source, σ_2, was set to range from 12.5 mm to 27.2 mm. For energies above 150.0 MeV, the second source was not needed. For energies lower than 80 MeV, the weight for the second source is set as 0.12. For energies from 80 MeV to 150 MeV, the weight of the second source is 0.08 [40, 51, 52].3D dose distribution of individual energy could be calculated by TOPAS by this simulation model.

4.2.3 Pre-stored Data Set

A data set includes the dose distribution matrices of all (94) total proton energies and is stored for matrix registration and reconstruction. Multiple dose distribution profiles are stored by matrices (Figure 4.1D). The new and decisive dose distribution matrix for a specific treatment plan is reconstructed by adding these individual dose distribution matrices together.

4.2.4 Matrix Registration And Reconstruction

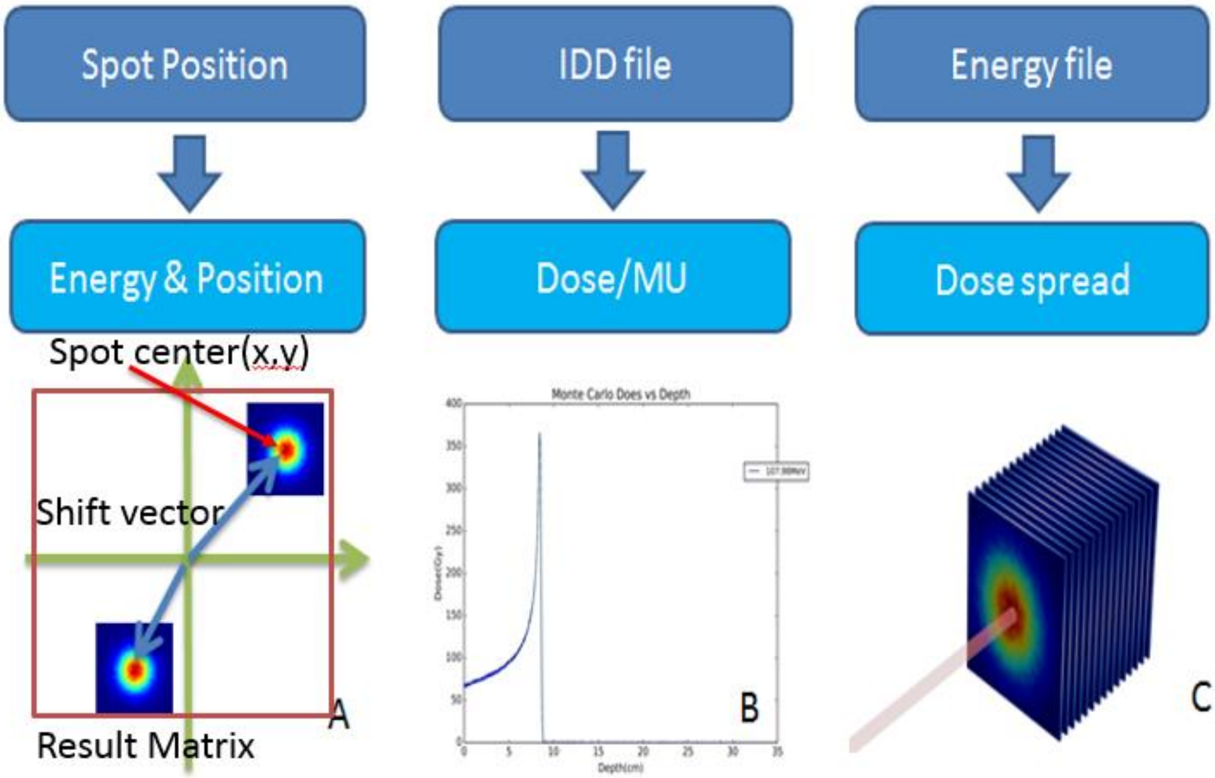

Figure 4.2 Fast dose caculation process

4.2.4.1 Definition Of Spot Position And Dose Distribution Matrix Registration Method

The longitudinal (z-direction) position of a spot is defined as the point where the integral depth dose (IDD) of a spot falls under 90% of the Bragg peak. This location is determined by x-x and y-y steering magnets in the lateral (x-y) direction and spot energy in longitudinal (z) direction (Figure 4.1C). The spot coordinates (x,y) are located at the position where the center of the dose distribution matrices of individual energy (SingleMatrix) locates in the result matrix (ResultMatrix). Dose distribution matrices of individual energy (SingleMatrix) are registered in the result matrices (ResultMatrix) by matching the center of the SingleMatrix to the spot position in the ResultMatrix (Figure 4.2A).

4.2.4.2 Matrix Reconstruct Method

In each patient's treatment plan, information regarding the spot coordinates and energy levels are drawn from the TPS dicom file. The dose distribution matrices of individual energy (SingleMatrix) are drawn from pre-stored data sets (Figure 4.2C). Dosage per unit is calculated by IDD measurement files for each energy (Figure 4.2B). These IDD measurement files are the commissioned data of the proton delivery system. Each individual dose distribution matrix is shifted to the position according to spot positions (Figure 4.2A). The result distribution matrix for a specific treatment plan is reconstructed by an equation (4.1) .Because the size of the individual dose distribution matrix (SingleMatrix) is 250×250 pixels, the coordinate range of SingleMatrix in the ResultMatrix is (x-125: x+125, y-125: y+125).

ResultMatrix [x-125: x+125, y-125: y+125] = ResultMatrix [x-125: x+125, y-125: y+125] +SingleMatrix (Eq 4.1)

Where:

- ResultMatrix is the new dose distribution matrix used to determine specific depth in a treatment plan.
- The spot coordinate(x,y) is the position where the center of dose distribution matrix of individual energy(SingleMatrix) locates in the result matrices (ResultMatrix).
- SingleMatrix is the dose distribution matrix of individual energy at specific depth. It is a 250x250 pixel matrix which corresponds to the sizable area in ResultMatrix.

4.2.5 Dose Calculation Results Validated By Clinical Treatment Plan

Quality assurance measurements contain two components: [1] dose measurements using the treatment fields delivered through the electronic medical record (EMR) system (Mosaiq versions, 1.5–2.4; Elekta Medical Systems, Sunnyvale, CA, USA) in the quality assurance mode and through the accelerator control system (ACS) in the treatment mode; and [2] extra dose measurements of depth dose and two-dimensional (2D) dose distributions at altered depths in the physics mode of the ACS. The measurement is implemented by Matrixx (MatriXXTM, Scanditronix Wellhofer, Schwarzenbruck, German) [65]. For methods used by Matrixx, refer to Section 1.1.6. The ResultMatrix, or the calculation result, will be validated by comparison to the measurement results acquired by the Matrixx gamma test (refer to Section 1.1.6).

4.3 Result

4.3.1 Calculation Results Validated By IDD Measurement Data

The integral depths of dosage (IDD) for all energies are calculated by the fast dose calculation method. The calculation data is compared with the measurement data acquired from commission data of the proton delivery system (Figure 4.3).All differences are within 3%. This accuracy satisfies our clinical requirement, which is a 3% dosage difference between calculation and measurement data.

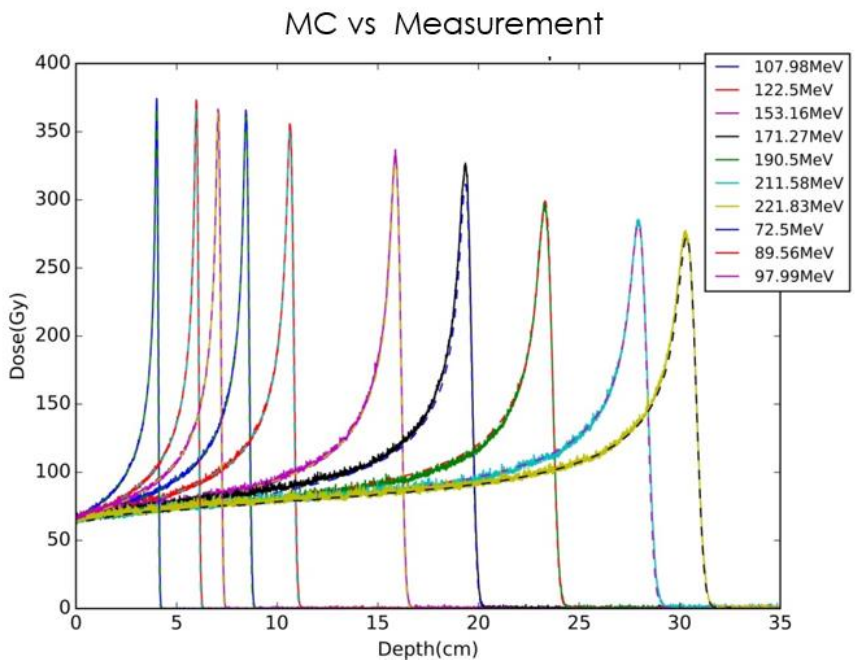

Figure 4.3 IDD data validation

4.3.2 Calculation Results Validated By Lateral Dose Distribution

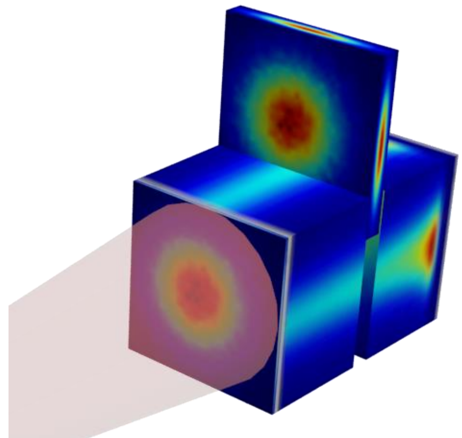

Figure 4.4 Schematic of lateral does distribution

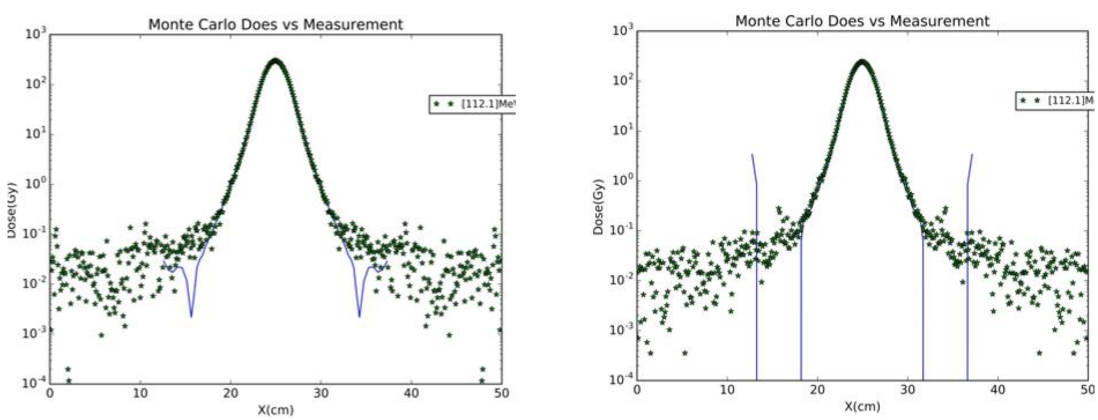

Figure 4.5 Lateral dose distribution validation

The reconstructed dose matrix in an x-y plane is validated by lateral dose distribution data acquired from commission data of the proton delivery system (Figure 4.4). The tolerance for this validation is 10^{-1} cGy. All differences for reconstructed dose matrices are compared to the measurement data and are within 3% (Figure 4.5). This level of accuracy satisfies our clinical requirements.

4.3.3 Calculation Results Validated By Clinical Plan

The calculation results (Figure 4.6A&C) are compared with measurement data from a treatment plan acquired by Matrixx (Figure 4.6B&D). According to Figure 4.6(E&F), the gamma test pass rate under the criteria of 3 mm – 3% amounts to 98.5%, which is much higher than our clinical requirement (Figure E&F).

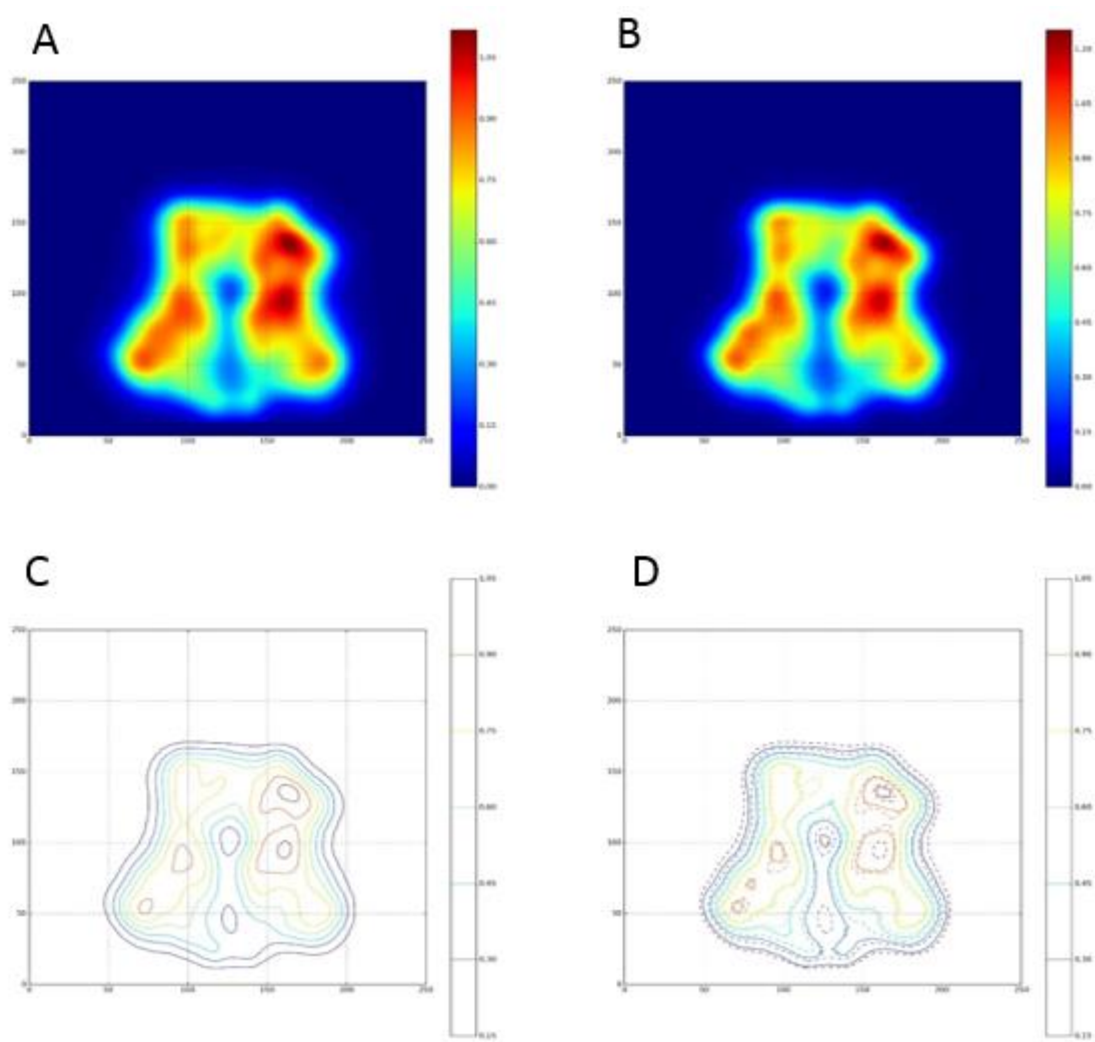

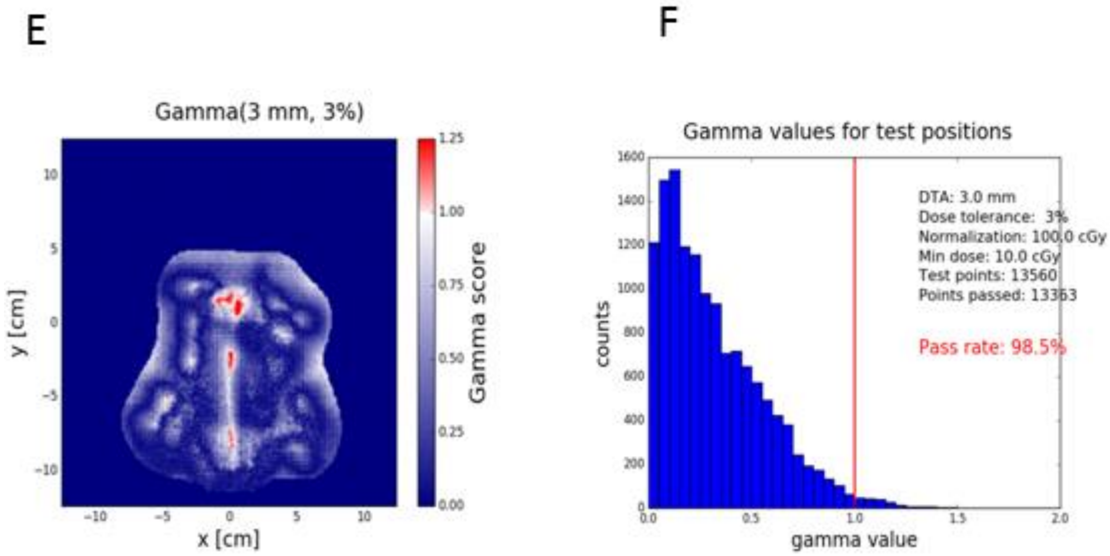

Figure 4.6 Caculation result validated by measurement data

Table 4.1 Calculation results validated by different treatment sites

Treatment site	Gamma pass rate
Brain	99.30%
Head&neck	98.50%
Lung	90.20%

Calculation results are validated by different treatment sites. The pass rates of these treatment plans are higher than 90% according to 3 mm – 3% criteria (Table 4.1).

4.3.4 Computational Efficiency Assessment

The average calculation time, based on (4) treatment plans, is 20 minutes per plan. Calculation time varies according to the number of spots found in the treatment plans. Time used is lower than the time required using tradition method in TOPAS, which is approximately (5) hours per plan [40].

4.4 Discussion

4.4.1 Dose Calculation Based On TOPAS Can Be Implemented On Personal Computer With Satisfying Efficiency

As reported by previous clinical publication, the calculation time for a beam during a typical head and neck exam is (4) CPU hours per million particles based on a sever (2.8-2.9 GHz Intel X5600) by TOPAS [40]. Fast dose calculation method is implemented on a personal computer (4GHz Intel i7-6770), where calculations for one treatment plan can be completed within 20 minutes. Gamma test results between calculation data and measurement data can satisfy our current clinical requirement 3mm -3% (90% pass rate).

4.4.2 The Method With More Flexibility

Based on the advantages of TOPAS, there is more flexibility with this method than with other analytical methods. The features of the model, such as SSD, phantom material, and architecture can be easily modified and tested. They all can be validated by common measurement data, including IDD and lateral dose distribution data.

4.4.3 Future Work

The proposed water phantom would take the place of the water phantom block used in daily measurement taking. In the future, this model could then be replaced by a patient phantom which has been reconstructed from dicom files. Therefore, this method has the potential to generate better results.

4.5 Conclusion

We have shown the advantages of the fast dose calculation method based on TOPAS. This method can be integrated for use in clinical procedures. Both efficiency and accuracy match the current standard clinical requirements. The fast dose calculation method can be validated by the various treatment sites from proton treatment plans. A total of all validation results would satisfy clinical requirements. It is reasonable to conclude that the fast dose calculation method in proton treatment analysis system can reduce labor costs and improve efficiency in both clinical practice and the academic arena.

5 Proton Treatment Monitoring Through Circulating Tumor Cell Detection And Isolation By Regional Automatic Threshold And Image Registration Algorithm

5.1 Introduction

Proton treatment usually lasts 3 months. The status of a tumor could change significantly during this time. According to current research, Circulating Tumor Cells (CTCs) are considered one of the best choices for monitoring tumor status. The mechanism describing how nanostructured embedded microchips could immobilize and isolate CTCs was discussed in our previous research report [24]. A CTC analysis program, based on regional automatic threshold and image registration algorithms, could automatically detect and isolate CTCs from nanostructured embedded microchips has been developed for monitoring the status of tumors during the proton treatment process.

Nikon Digital Microscope and Laser Capture Microdissection (LCM) are systems used to detect and isolate CTCs from microchips. The Nikon Digital Microscope system scans high-quality images to detect CTCs on nanostructured embedded microchips. The LCM system could provide qualified genetic analysis of tumor cells [66, 67]. It is widely used in rare cell isolation, heterogeneity of tissue separation, and circulating DNA separation [68] [69].

The degree of automation in the Nikon Digital Microscope and LCM systems is very low, making them valuable in clinical practice. Before the CTC analysis program developed, researchers were required to manually recognize and isolate CTCs from thousands of cells on the microchips. This resulted in labor that was time-consuming and tedious, yielding subjective and imprecise results. Therefore, these systems could aid in the efficiency of monitoring the tumor status during proton treatment.

5.2 Materials And Methods:

5.2.1 Materials

5.2.1.1 Q Program

Q Programming language is applied directly in order to control computer operation. The Q program script will link to the keyboard of a computer to operate software for the Laser Capture Microdissection system (LCM). Together, Q program script and the LCM software control a laser used to cut out a specific area based on input coordinates.

5.2.1.2 Laser Capture Microdissection System (LCM)

The Laser Capture Microdissection system (LCM) is used to isolate single CTCs from microchips for molecular analysis. LCM isolates single CTCs with genetic material of a high purity for second-generation deep gene sequencing [69]. LCM includes the following devices:

- Nikon Eclipse high resolution immunofluorescence microscope
- Hamamatsu C11440 high resolution camera
- Nikon Eclipse Ti-E high quality (inverted research) microscope
- Arcturus® LCM system
- Q programing language compiler
- PLGA NanoVelcro Chips

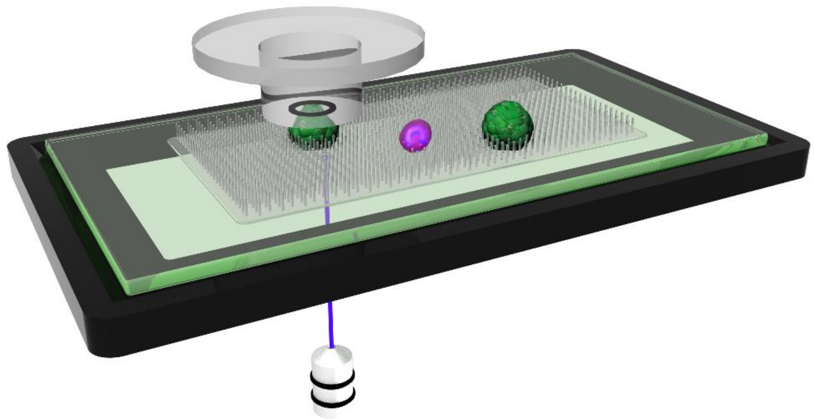

Figure 5.1 Micro Laser Dissection on micro-chip

5.2.2 Method:

There are 4 steps involved in monitoring tumor status via CTC analysis:

- The imaging condition parameter must be acquired in order to calculate the intensity adjustment factor (IAF) of immunofluorescence under different exposure times.
- The target area of the microchips must be scanned. High resolution CTC images are acquired for CTC analysis.
- CTCs are then detected in the images using a regional automatic threshold algorithm. Tumor status will be reported to medical professionals in order to create new treatment plans if morphological features related to tumor status, such as vsn (very small nuclear) CTCs are detected.
- Isolation of CTCs on the chips is completed by using an image registration algorithm. Positioning of the CTCs is acquired in Step 3: Single CTCs are harvested in this step and could be used for molecular analysis while monitoring tumor status.

5.2.2.1 Imaging Condition Parameter

Table 5.1 Imaging condition testing List

Concentration \Time	01:00.5	1:01	1:02	1:00	
	1	2	3	4	
5 mins	A1	A2	A3	A4	A
10 mins	B1	B2	B3	B4	B
30 mins	C1	C2	C3	C4	C
1h	D1	D2	D3	D4	D
2h	E1	E2	E3	E4	E

Exposure time is an important parameter on acquiring fluorescence image. The relationship between fluorescence intensity and exposure time are clarified by the test. Because the intensity adjust factor (IAF) is a relative value, varies in different laboratories. CTC characteristics include the size of the nucleus, cell size is related with cell immobilization methods, solution concentration and other experimental conditions. Intensity adjust factor should be re-calibration in different experimental condition.

Standard Immunofluorescence test are applied to 3-color immunocytochemistry (ICC) protocol for equivalent staining of DAPI, FITC-labeled anti-CK, TRICY-labeled anti-CD45 [27].The immunofluorescence intensity is related to the antibody concentration and stain time. The intensity adjust factor (IAF) is calculated by slope of linear relationship equation of immunofluorescence and exposure time.

5.2.2.2 Automatic Scan Images On Nickon 90i Imaging System

The parameters setting according our previous test [70].Intensity adjust factor (IAF) is based on imaging condition parameter in 5.2.2.1(Figure 5.2).

High resolution images are scanned on the chip based on following scanning parameters:

The fluorescence of target area is set from 30 to300 and the circularity of target area is set from 0.65 to 1.00.

- TRICT<200×IAF of TRICT
- FITC > 200×IAF of FITC
- DAPI>200×IAF of DAPI

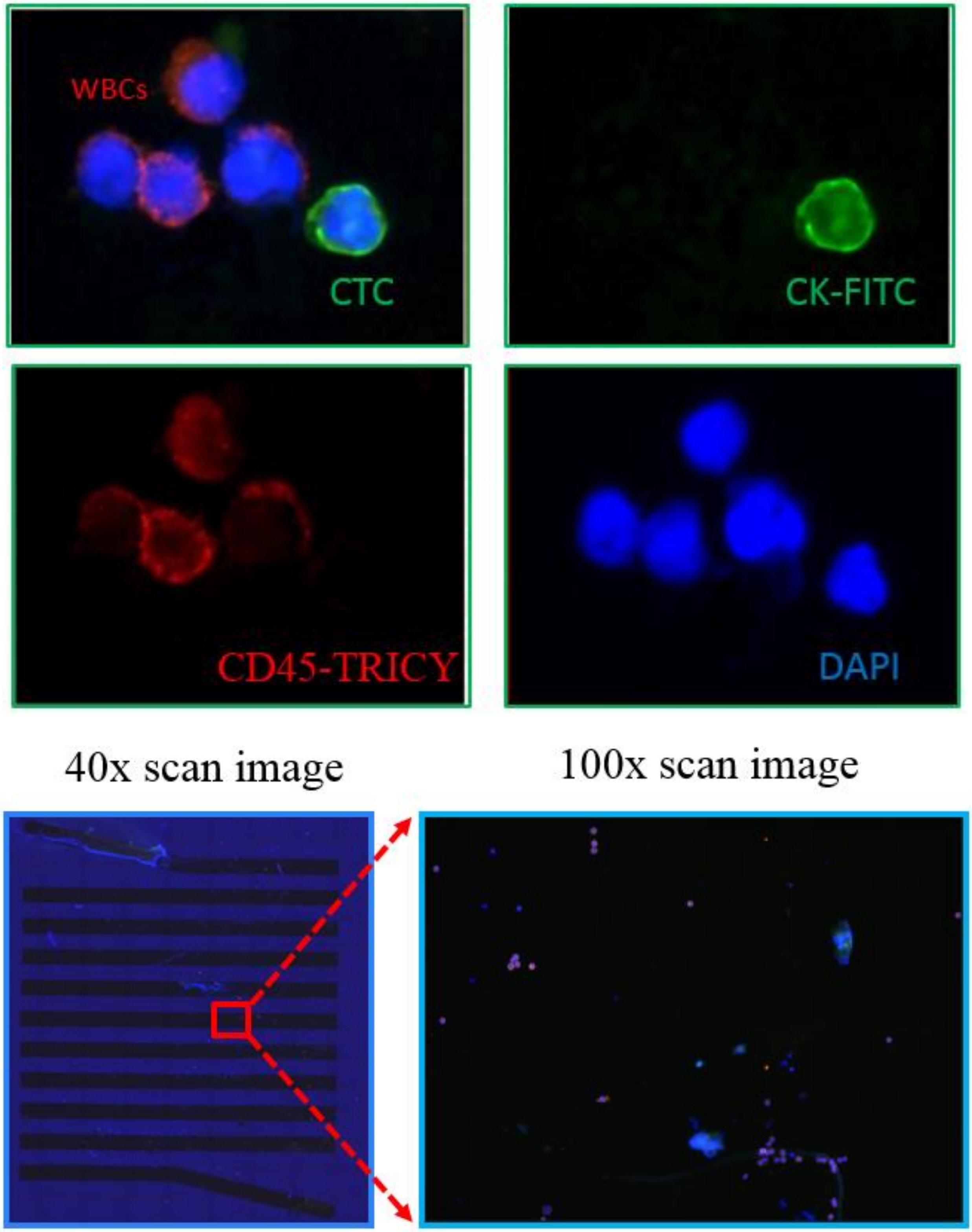

Figure 5.2 Images scanned by Nickon imaging system

The image in Figure 5.2 includes three channels:

- Green channel stands for FITC which is conjoined with CTCs membrane biomarker
- Red channel stands for TRICT which is conjoined with white blood cell
- Blue channel stands for DAPI which is nuclear biomarker

5.2.2.3 Regional Automatic Threshold Algorithm

All algorithms are implemented in Matlab R2014a.The automatic threshold algorithms is a function from Matlab imaging toolbox.

Regional automatic threshold is applied on scanning images. The algorithm applies automatic threshold on all three channels of the images and then merge the region of interest (ROI) of FITC and DAPI which represent for cell membrane and nucleus (step 2 equation). Then enlarge the area by 5 times to acquire the target area.5 times area is applied here based on the average distance between cells is five times of cell diameter. Automatic threshold method are applied to individual area for segmenting the cell structure locally.

The algorithm could be described as following steps.

1. Apply automatic threshold to 2 channels (Figure 5.3)

2. ROI(Region of interest)= $(DAPI \cap FITC \cap \neg TRICY)*5$(Figure 5.4)

3. Apply Automatic threshold on Individual ROI for each channel (Figure 5.4)

4. Register the ROI in Figure 5.4 by position to the original image, CTCs position are marked out (Figure 5.5)

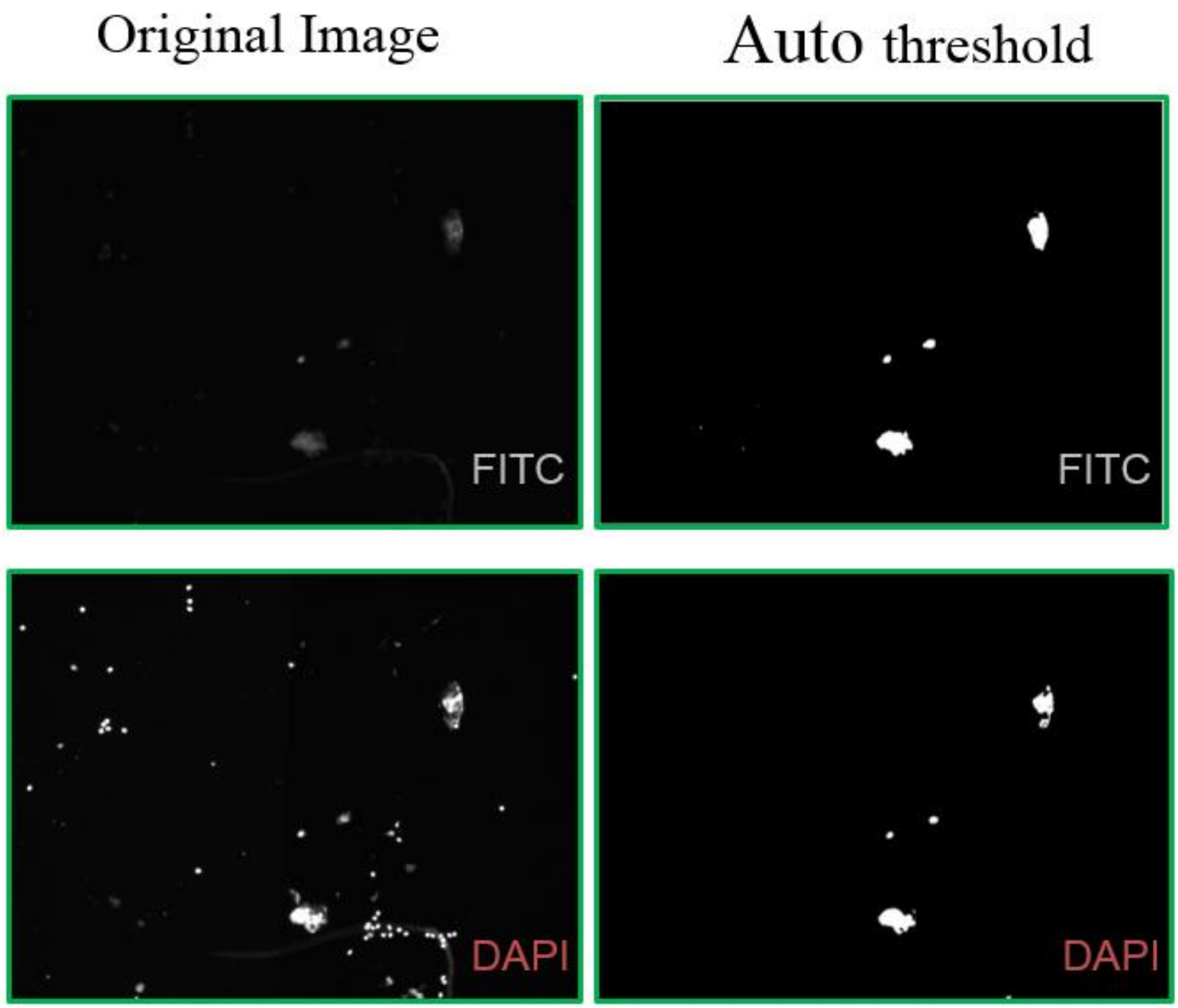

Figure 5.3 Automatic threshold on FITC and DAPI channel

Figure 5.4 Region of interest result by merging information from FITC and DAPI area

CTC 1 CTC 2

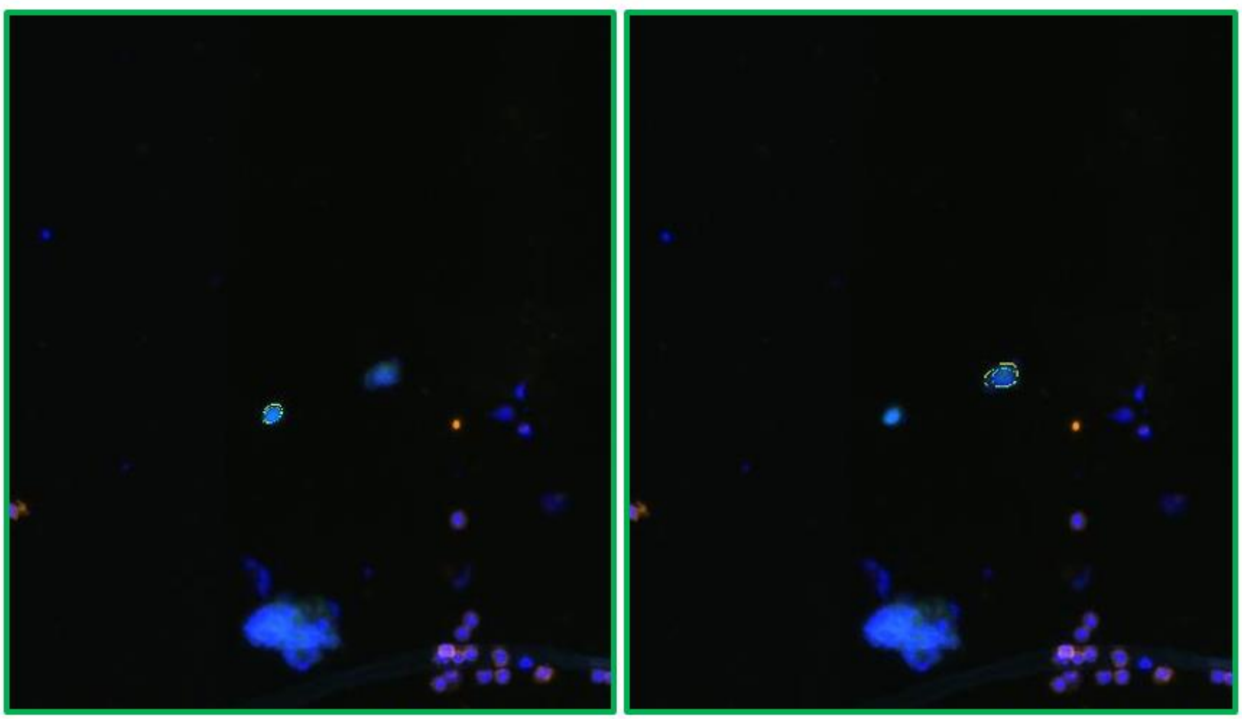

Figure 5.5 CTCs detected by CTCs analysis program, the yellow outline is cell membrane, green outline is the cell Nucleus

5.2.2.4 CTC Isolation Algorithms

Images with marked CTCs position (X_p,Y_p), Figure 5.6A. Cell center position (X_p,Y_p) is acquired by regional Automatic Threshold.

Cell center position (X_p,Y_p) registered on the full scan image position (X_i,Y_i) by following equation(Figure 5.6B):

$$X_i = X_p * N$$

$$Y_i = Y_p * M$$

(M,N) is the image scan sequence number acquired from the scan images files in Figure 5.6B.

The full scan image position of (X_i,Y_i) is registered on the chip position (X,Y) by the following equation (Figure 5.6C):

$$X = ((X_i - X_0)/123) + 294$$

$$Y = ((Y_i - Y_0)/123) + 839$$

(X_i,Y_i) is the coordinate of the full scan image under the C11440 high resolution camera. (X_0,Y_0) is the reference point and (X, Y) is the coordinate that will be used for registration on the chip. (294,839) is the reference point on the LCM screen.

(X,Y) is based on the screen coordinate; the resolution of the screen will affect the registration on the LCM (for example, every time the screen changes, the reference point on the LCM will also change).

Q program script will operate the laser to cut a circle with (X, Y) as the center on the microchip. CTCs on the cut area will be collected by caps covering the microchip. The caps contain a sticky substance that clings to the surface of the microchips.

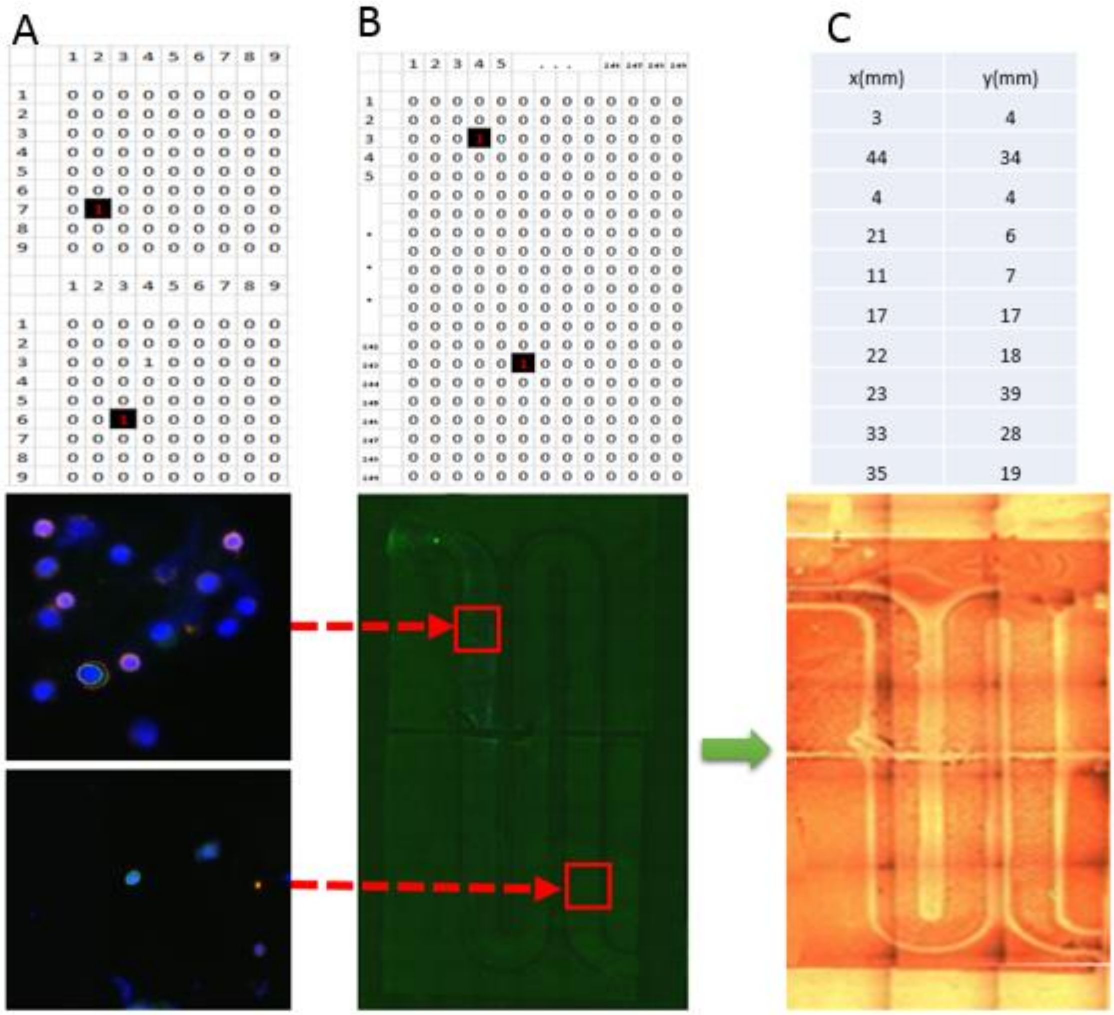

Figure 5.6 A is the target cells detected by the detection system. The cell center position is marked out by a binary matrix (black area) in local image. B is the cell's center position registered on the full scan image of the chip. C is the cell's center position on the LCM system.

5.2.2.5 CTCs Viability Validation By Housekeeping Genes Test

Cells on the caps will be processed by the Qiagen whole genome amplification (WGA) kit. The genetic material of the cells will be amplified by the kit for housekeeping genes test. A multiplex PCR reaction of a panel of 8 housekeeping genes (located at different chromosomes) is employed to validate CTCs viability. After the multiplex PCR reaction, only those samples which exhibited positive readout (as in, more than 5 out of the 8 housekeeping genes are positive) will be considered as qualified cells.

5.3 Result And Discussion

5.3.1 Imaging Condition Parameter

According to the results, a regression curve is plotted and shown in Figure 5.7 and Figure 5.8. Fluorescence intensity has a significant correlation to exposure time. The coefficient ‘a’ correlates to the density of the antibody on the cell membrane. This coefficient ‘a’ is issued as the intensity adjust factor (IAF). The P-value is low for y 0 because it is related to the background condition variable. The values of y 0 equal the background value when the exposure time is 0. This is a critical value for further image processing, as some of the criteria for CTC detection states that FITC intensity shall double that of the background intensity. A similar regression curve of DAPI is shown in Figure 5.9.

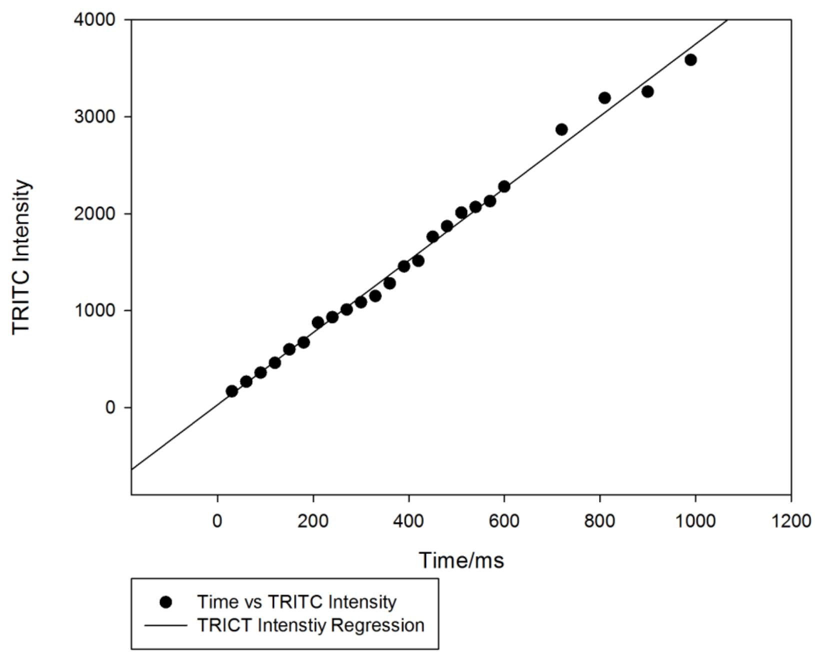

Figure 5.7 Exposure time and the correlation curve of the TRICY fluorescence intensity

Equation: Polynomial, Linear

$$f = y_0 + a \times x$$

Table 5.2 TRICY fluorescence equation factor

	R	Rsqr	Adj Rsqr	Standard Error of Estimate
	0.9971	0.9942	0.9939	76.7869
	Coefficient	**Std. Error**	**t**	**P**
y_0	29.7602	29.0862	1.0232	<0.3173
a	3.7178	0.0605	61.4532	<0.0001

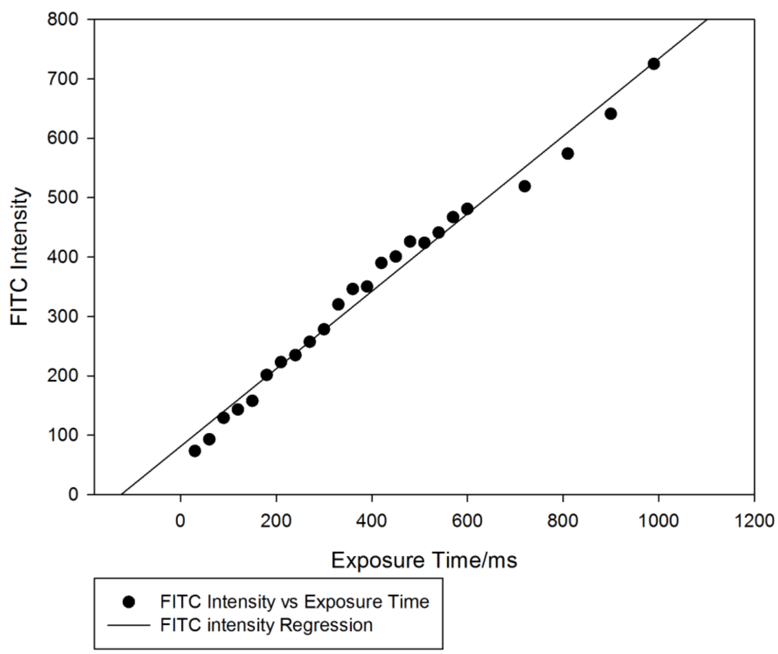

Figure 5.8 Exposure time and the correlation curve of the FITC fluorescence intensity

Equation: Polynomial, Linear

$$f = y_0 + a \times x$$

Table 5.3 FITC fluorescence intensity equation factor

	R	Rsqr	Adj Rsqr	Standard Error of Estimate
	0.9925	0.9851	0.9844	21.7294
	Coefficient	Std. Error	t	P
y_0	81.5271	8.2309	9.905	<0.0001
a	0.6521	0.0171	38.0924	<0.0001

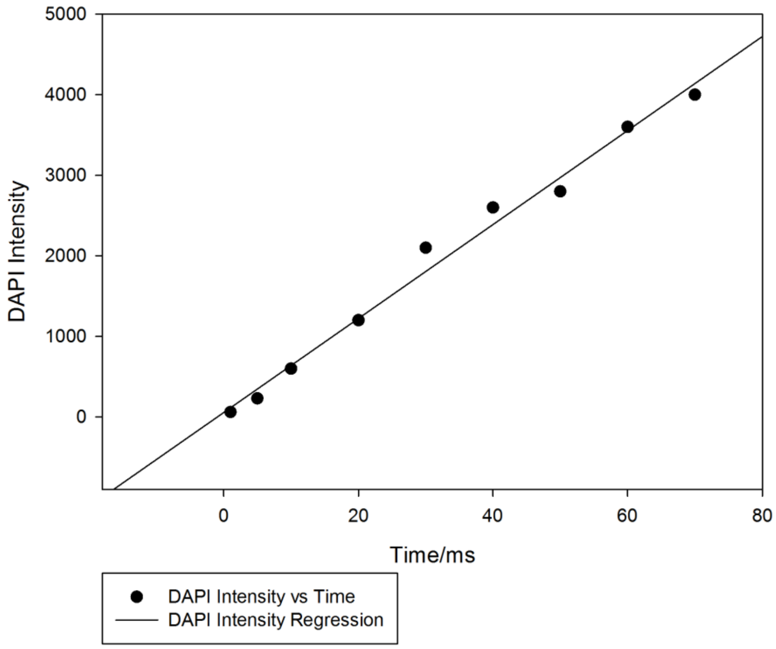

Figure 5.9 Exposure time and the correlation curve of the DAPI fluorescence intensity

$$f = y_0 + a \times x$$

Table 5.4 DAPI fluorescence intensity equation factor

	R	Rsqr	Adj Rsqr	Standard Error of Estimate
	0.9941	0.9882	0.9865	169.384
	Coefficient	Std. Error	t	P
y_0	56.773	95.1617	0.5966	<0.5696
a	58.3183	2.4106	24.1929	<0.0001

5.3.1.1 Relationship Between Imaging Result And Antibody Concentration

The antibody concentration rate (1X, 2X) is based on ThermoFisher cytokeratin standard dilution procedure.

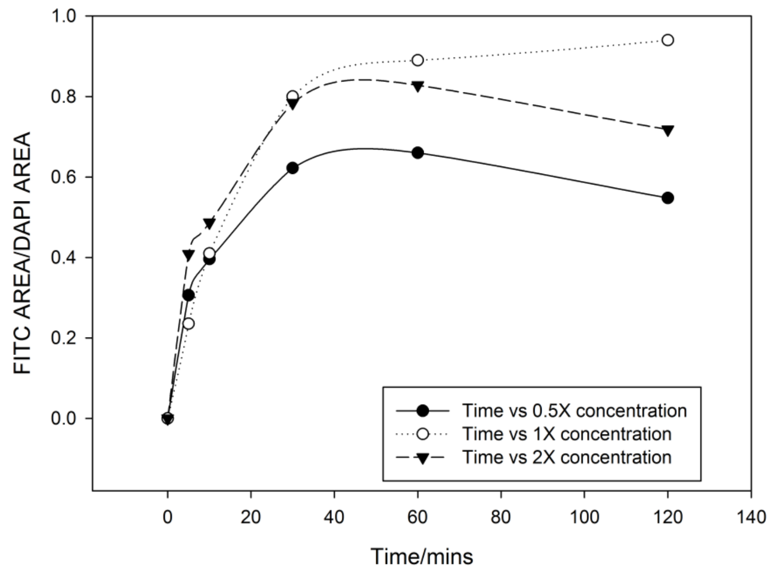

Figure 5.10 FITC Area/DAPI Area Curve

Because the FITC label on cytokeratin shows the reaction of an antibody combining with the antigen on the cell membrane, the FITC area represents the membrane with cytokeratin protein. DAPI is always applied to this area. According to principles of DAPI application, we assume that the nucleus and the area marked by DAPI is a fixed value for each cell under any given condition. The FITC/DAPI rate stands for the cytokeratin relative to the stained area. According to Figure 5.10, the FITC/DAPI rate peaks at 40 minutes. A comparison of the 0.5X concentration to the 1.0X concentration of an antibody shows that a higher concentration could enlarge the stain area. However, a 1.0X concentration is sufficient since the FITC stain area showed no improvement after the application of a 2.0X concentration antibody.

5.3.1.2 Relationship between Antibody Concentration and Background Fluoresce Intensity

The intensity difference between FITC and background TRITC characterize the signal noise ratio (Figure 5.11). The value reaches its peak at 40 mins. The 2X concentration antibody solution did the best signal noise ratio. The curve varies randomly after 40 minutes.2X concentration antibody could be used to acquire best signal. The staining time shall be limited within 40 minutes.

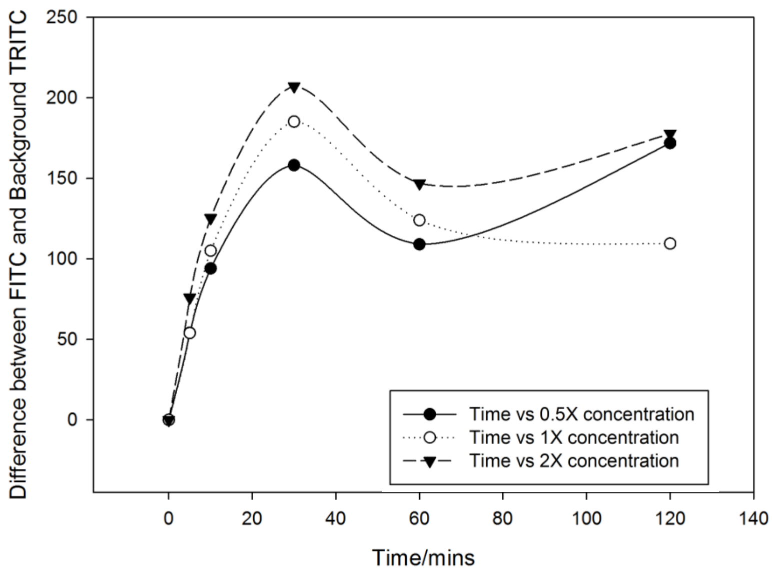

Figure 5.11 Difference between FITC and Background TRICY

5.3.1.3 Relationship between Antibody Concentration and Non-specific Staining

According to Figure 5.12, the TRICY fluorescence intensity from a tumor cell reflects non-specific staining on the cell membrane due to the non-existence of white blood cells. Non-specific staining is the reason why TRICY, a white blood cell biomarker, may combine with CTCs. This phenomenon has always existed, but immunophenotype can still be distinguished if the FITC intensity divided by the TRICY intensity is higher than two. The ratio reaches its peak at 40 minutes, decreasing significantly after that. The highest ratio appears when the antibody concentration is at 1.0X.

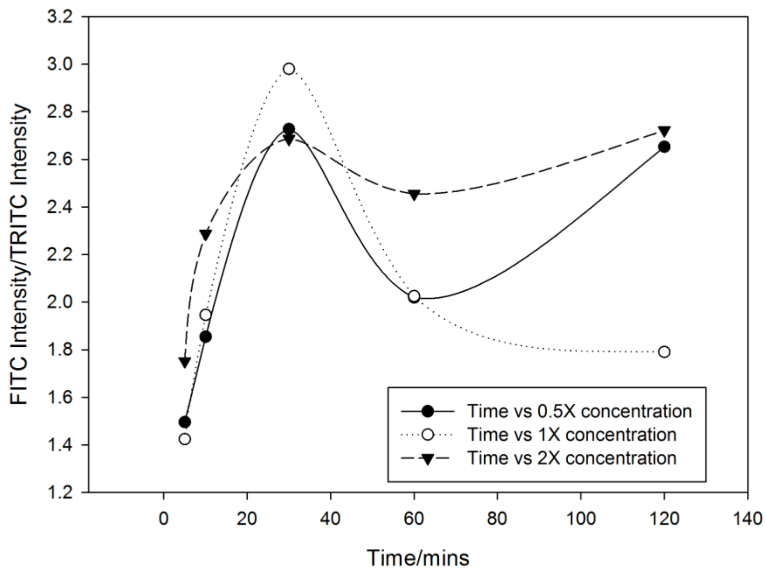

Figure 5.12 FITC/TRICY ratio

5.3.1.4 Imaging Conditions Required By CTCs Analysis Program

Intensity adjust factor (IAF) for all biomarkers shall be acquired and applied to adjust fluoresce intensity according to the exposure time. The staining time shall be within 40 minutes to get best signal /noise ratio. Our current antibody concentration (1X) could acquire best CTCs staining signal and prevent non-specific staining. This concentration of antibody will be required for any input images to the CTCs analysis program.

5.3.2 Region Of Interest Detection

The circles displayed in Figure 5.13 marked out the regional of interest. CTCs in these ROI will be detected by regional automatic threshold algorithm.

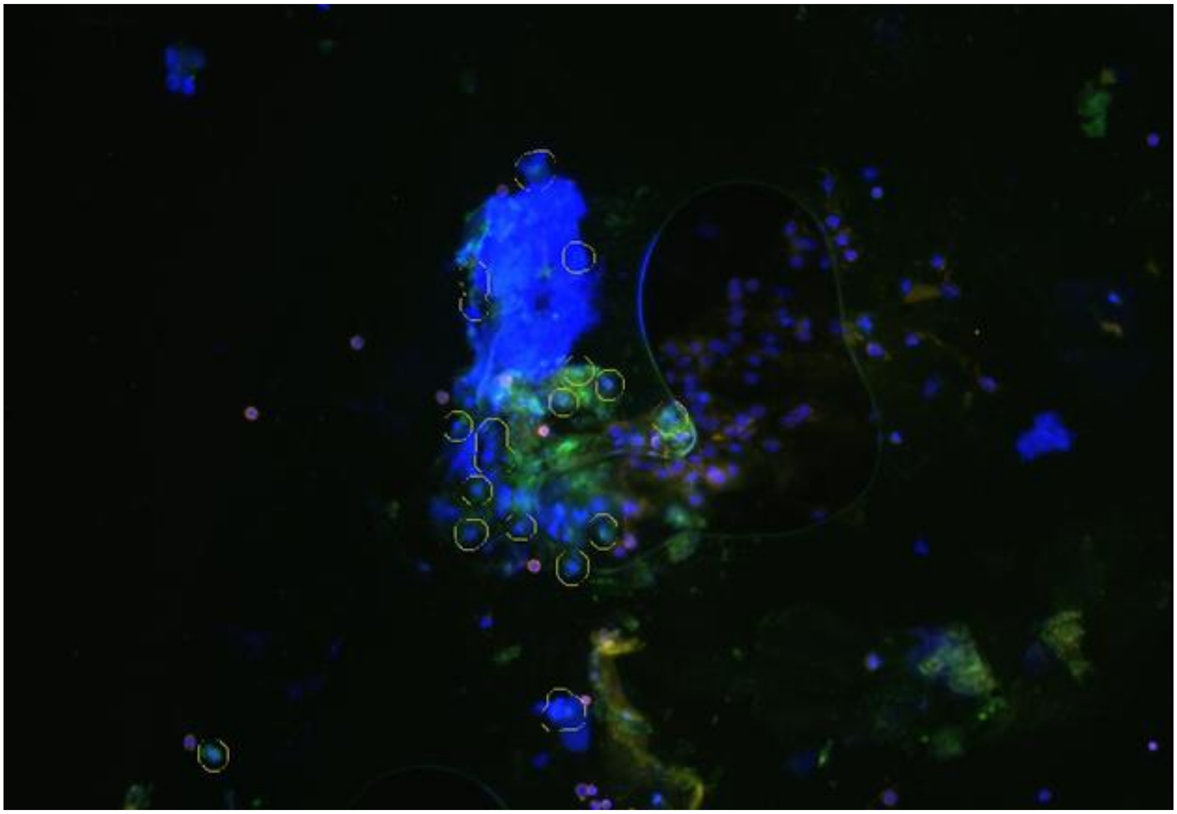

Figure 5.13 Region of Interest, the yellow outline marked out the segmented region

The features of CTCs are acquired by a regional automatic threshold. According to our analysis of the morphological features of CTCs the sub-classification of prostate cancer, based on circulating tumor cells classified by nuclear size, reveals the existence of very small nuclear circulating tumor cells in patients having visceral metastases.

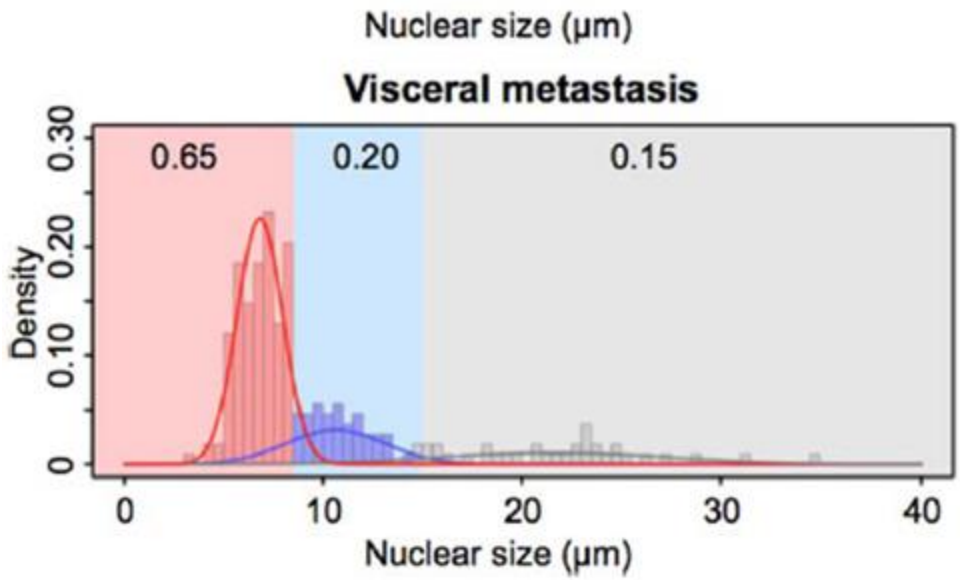

Figure 5.14 visceral metastasis, in which vsnCTCs account for the largest percentage of cells (65%)[71].

The revelation between vsnCTC(very small nuclear) and visceral metastases was reported in our previous clinical research publication[71].VsnCTC were found to be elevated in patients with visceral metastases compared with without vsnCTC(0.3660.69 vs 1.9563.77 cells/mL blood; $P<0.001$)(Figure 5.14). CTCs automatic analysis program will signal physicians to modify proton treatment plan whenever vsnCTC are detected.

5.3.3 CTCs Automatic Isolation

5.3.3.1 Speed Of Cell Harvest

The average time spent on 1 chip is 30 minutes by human operation versus 15 minutes via the automatic analysis program. If there are two LCMs, it is possible for one technician to operate two machines in the same time thereby improving the efficiency two fold.

5.3.3.2 CTCs Viability Validation

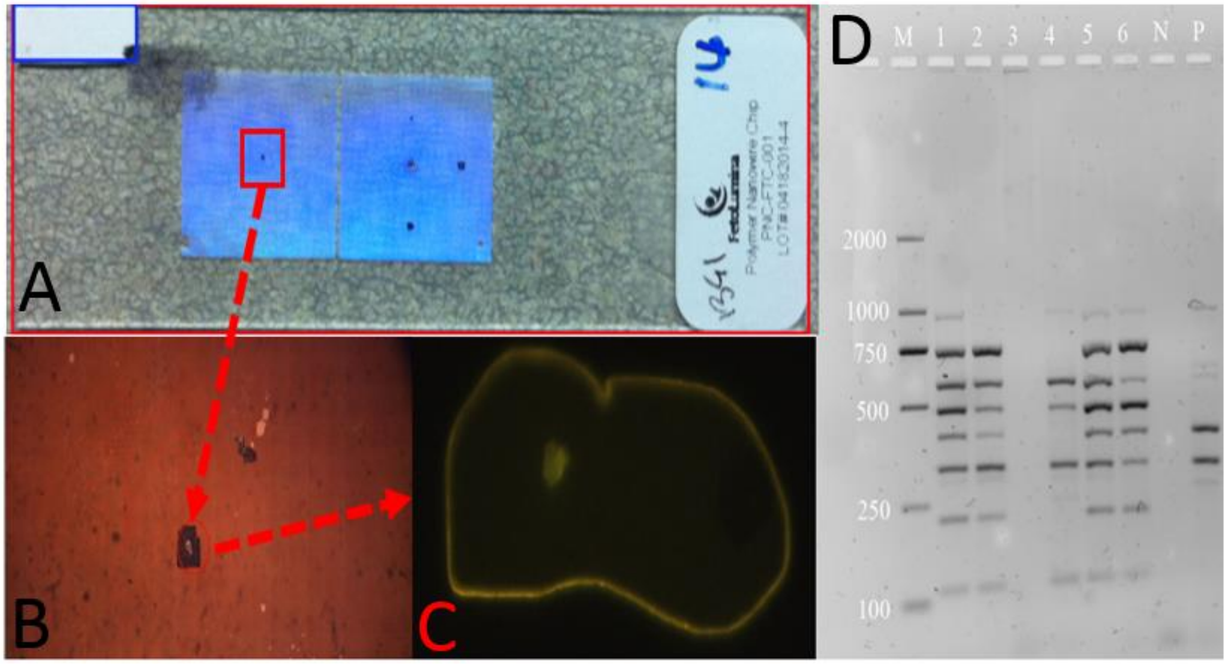

Figure 5.15 A is LCM standard micro-chip. B is cut area on LCM system. C is the target cell with green immunofluorescence on cut off area is housekeeping test result of the cut off cells.

According to Figure 5.15B, the red circle area is the area cut off from the chip by laser. The target cell with immunofluorescence (Figure 5.15C) is shown inside the cut area. According to Figure 5.15D, the six cells cut by the system (all of the cells with the exception of channel 3) are considered qualified cells for further molecular analysis. The results prove that the CTCs automatic analysis system could adequately protect cell viability for tumor status monitoring.

5.4 Conclusion

CTCs can be effectively detected by a regional automatic threshold algorithm under the conditions describe in section (5.3.1.4). Characteristics (such as very small nucleus) can be used to monitor the metastasis of a tumor. Medical doctors are then able to adjust treatment plans according to the information received from a tumor status. The automatic LCM control program greatly improves efficiency during cell harvesting, while cell viability remains well protected during molecular analysis. Molecular features could provide additional information regarding tumor status. Overall, the CTC analysis program in proton treatment analysis system is valuable in monitoring tumor status through its use of morphological features and through isolation of single high viability CTC.

6 Conclusion

This study focused on applying automatic analysis technology to proton therapy treatment. Segmentation and registration algorithms (including matrix registration by proton spot positioning, connected-component algorithms, regional automatic threshold, and image registration by CTC positioning) are used to analyze proton treatment plans. The main objective is to reduce labor and time during the treatment process.

The biggest range shifter correction factor is 0.11, which could significantly affect the dose calculation results. The mean dose difference (between the range shifter model simulation results and the measurement results acquired by the Bragg's peak chamber) is within 1.3%. This dose difference satisfies our clinical requirement of being within 3%.

Small spot cluster analysis is able to detect 100% of the revised treatment plans involving sites such as the head and neck, thorax, and 4D thorax. Error revision of treatment plans could be completed before measurements are taken with the help of small spot cluster analysis, thus saving time and labor.

Fast dose calculations based on pre-stored simulation data in matrices can be used to reconstruct new dose distribution matrices, according to the position of spots in imaging seen in the treatment plan. Calculations could be completed in less than 30 minutes per beam on a personal computer and may be deployed from any location. Even if the original model is modified, a new data set could be built within a few days. The dose calculation results are validated by clinical treatment plans. Gamma test pass rates for all treatment plans are higher than 90%, which satisfies clinical requirements.

Circulating Tumor Cell analysis could provide feedback for physicians to adjust treatment plans without requiring invasive screening methods. VsnCTCs account for the largest percentage of cells (65%) in visceral metastasis. The CTC automatic analysis program could guide medical professionals in adjusting treatment plans by detecting features such as vsnCTCs.

Overall, the automatic proton treatment analysis system greatly improves the efficiency during the proton treatment process. Perhaps the largest contribution is the conservation of labor and redundant work, making it highly valuable in a clinical setting.

Reference

1. Siegel, R., D. Naishadham, and A. Jemal, *Cancer statistics, 2013.* CA Cancer J Clin, 2013. **63**(1): p. 11-30.

2. *StatBite: Particle beam therapy facilities worldwide.* J Natl Cancer Inst, 2010. **102**(7): p. 451.

3. Wilson, R.R., *Radiological use of fast protons.* Radiology, 1946. **47**(5): p. 487-91.

4. Walton, E.L., *Positive perspectives from proton therapy.* Biomed J, 2015. **38**(5): p. 361-4.

5. Shukla, M.K. and J. Leszczynski, *Hydration-dependent structural deformation of guanine in the electronic singlet excited state.* J Phys Chem B, 2008. **112**(16): p. 5139-52.

6. Lomax, A.J., *Intensity modulated proton therapy and its sensitivity to treatment uncertainties 2: the potential effects of inter-fraction and inter-field motions.* Phys Med Biol, 2008. **53**(4): p. 1043-56.

7. Paganetti, H., *Changes in tumor cell response due to prolonged dose delivery times in fractionated radiation therapy.* Int J Radiat Oncol Biol Phys, 2005. **63**(3): p. 892-900.

8. Eclipse. *https://www.varian.com/oncology/products/software/treatment-planning/eclipse-treatment-planning-system*. Available from: https://www.varian.com/oncology/products/software/treatment-planning/eclipse-treatment-planning-system.

9. Raaijmakers, C.P. and J. Welleweerd, *Comparison of treatment planning systems using the AAPM radiation therapy committee TG-23 test package. American Association of Physicists in Medicine.* Med Phys, 2000. **27**(3): p. 620-1.

10. M.Bues. *http://slideplayer.com/slide/1691947/*. Available from: http://slideplayer.com/slide/1691947/.

11. Wang, N., A. Ghebremedhin, and B. Patyal, *Commissioning of a proton gantry equipped with dual x-ray imagers and a robotic patient positioner, and evaluation of the accuracy of single-beam image registration for this system.* Med Phys, 2015. **42**(6): p. 2979-91.

12. Zhu, X.R., et al., *Towards effective and efficient patient-specific quality assurance for spot scanning proton therapy.* Cancers (Basel), 2015. **7**(2): p. 631-47.

13. Lu, G., et al., *Dosimetry in MARS spectral CT: TOPAS Monte Carlo simulations and ion chamber measurements.* Australas Phys Eng Sci Med, 2017.

14. Criscitiello, C., C. Sotiriou, and M. Ignatiadis, *Circulating tumor cells and emerging blood biomarkers in breast cancer.* Curr Opin Oncol, 2010. **22**(6): p. 552-8.

15. Yoon, H.J., M. Kozminsky, and S. Nagrath, *Emerging role of nanomaterials in circulating tumor cell isolation and analysis.* ACS Nano, 2014. **8**(3): p. 1995-2017.

16. de Bono, J.S., et al., *Circulating tumor cells predict survival benefit from treatment in metastatic castration-resistant prostate cancer.* Clin Cancer Res, 2008. **14**(19): p. 6302-9.

17. Lowes, L.E. and A.L. Allan, *Recent advances in the molecular characterization of circulating tumor cells.* Cancers (Basel), 2014. **6**(1): p. 595-624.

18. Khoo, B.L., et al., *Clinical validation of an ultra high-throughput spiral microfluidics for the detection and enrichment of viable circulating tumor cells.* PLoS One, 2014. **9**(7): p. e99409.

19. Pantel, K., R.H. Brakenhoff, and B. Brandt, *Detection, clinical relevance and specific biological properties of disseminating tumour cells.* Nat Rev Cancer, 2008. **8**(5): p. 329-40.

20. Cristofanilli, M., *Circulating tumor cells, disease progression, and survival in metastatic breast cancer.* Semin Oncol, 2006. **33**(3 Suppl 9): p. S9-14.

21. Louha, M., et al., *Spontaneous and iatrogenic spreading of liver-derived cells into peripheral blood of patients with primary liver cancer.* Hepatology, 1997. **26**(4): p. 998-1005.

22. Chambers, A.F., A.C. Groom, and I.C. MacDonald, *Dissemination and growth of cancer cells in metastatic sites.* Nat Rev Cancer, 2002. **2**(8): p. 563-72.

23. Yu, M., et al., *Circulating tumor cells: approaches to isolation and characterization.* J Cell Biol, 2011. **192**(3): p. 373-82.

24. Lin, M., et al., *Nanostructure embedded microchips for detection, isolation, and characterization of circulating tumor cells.* Acc Chem Res, 2014. **47**(10): p. 2941-50.

25. Gillin, M.T., et al., *Commissioning of the discrete spot scanning proton beam delivery system at the University of Texas M.D. Anderson Cancer Center, Proton Therapy Center, Houston.* Med Phys, 2010. **37**(1): p. 154-63.

26. Smith, A., et al., *The M. D. Anderson proton therapy system.* Med Phys, 2009. **36**(9): p. 4068-83.

27. Cao, W., et al., *Incorporating deliverable monitor unit constraints into spot intensity optimization in intensity-modulated proton therapy treatment planning.* Phys Med Biol, 2013. **58**(15): p. 5113-25.

28. Fix, M.K., et al., *Macro Monte Carlo for dose calculation of proton beams.* Phys Med Biol, 2013. **58**(7): p. 2027-44.

29. Armstrong, T.W. and K.C. Chandler, *Calculation of the dose, radionuclide production and delayed photon leakage due to solar-proton bombardment of tissue with potential application to astronaut dosimetry.* Health Phys, 1972. **23**(2): p. 159-67.

30. Low, D.A., et al., *A technique for the quantitative evaluation of dose distributions.* Med Phys, 1998. **25**(5): p. 656-61.

31. Schneider, U., E. Pedroni, and A. Lomax, *The calibration of CT Hounsfield units for radiotherapy treatment planning.* Phys Med Biol, 1996. **41**(1): p. 111-24.

32. Moyers, M.F., et al., *Ion stopping powers and CT numbers.* Med Dosim, 2010. **35**(3): p. 179-94.

33. !!! INVALID CITATION !!! .

34. Farace, P., et al., *Technical Note: A direct ray-tracing method to compute integral depth dose in pencil beam proton radiography with a multilayer ionization chamber.* Med Phys, 2016. **43**(12): p. 6405.

35. Zhang, X., et al., *Parameterization of multiple Bragg curves for scanning proton beams using simultaneous fitting of multiple curves.* Phys Med Biol, 2011. **56**(24): p. 7725-35.

36. Djouguela, A., et al., *The dose-area product, a new parameter for the dosimetry of narrow photon beams.* Z Med Phys, 2006. **16**(3): p. 217-27.

37. Mirandola, A., et al., *Dosimetric commissioning and quality assurance of scanned ion beams at the Italian National Center for Oncological Hadrontherapy.* Med Phys, 2015. **42**(9): p. 5287-300.

38. J. Hartman, X.Z., X. R. Zhu, S.J. Frank, J.J.W. Lagendijk1, M. van Vulpen,and B.W. Raaymakers. *MODELING OF MD ANDERSON SCANNING PROTON BEAM FOR QUALITY ASSURANCE IN INTENSITY MODULATED PROTON THERAPY AND MRI-GUIDED PROTON THERAPY SIMULATIONS*. 2016; Available from: http://www.umcutrecht.nl/getmedia/c6b9ac6e-1cce-4dc3-ac83-88feaffbe30c/201605_Poster_PTCOG_FINAL.pdf.aspx.

39. Perl, J., et al., *TOPAS: an innovative proton Monte Carlo platform for research and clinical applications.* Med Phys, 2012. **39**(11): p. 6818-37.

40. Ramos-Mendez, J., et al., *A framework for implementation of organ effect models in TOPAS with benchmarks extended to proton therapy.* Phys Med Biol, 2015. **60**(13): p. 5037-52.

41. Agostinelli, S., et al., *GEANT4-a simulation toolkit.* Nuclear Instruments & Methods in Physics Research Section a-Accelerators Spectrometers Detectors and Associated Equipment, 2003. **506**(3): p. 250-303.

42. Allison, J., et al., *Geant4 developments and applications.* Ieee Transactions on Nuclear Science, 2006. **53**(1): p. 270-278.

43. Guan, F., et al., *Spatial mapping of the biologic effectiveness of scanned particle beams: towards biologically optimized particle therapy.* Sci Rep, 2015. **5**: p. 9850.

44. Guan, F., et al., *Analysis of the track- and dose-averaged LET and LET spectra in proton therapy using the geant4 Monte Carlo code.* Med Phys, 2015. **42**(11): p. 6234-47.

45. Taleei, R., et al., *Monte Carlo simulations of (3)He ion physical characteristics in a water phantom and evaluation of radiobiological effectiveness.* Med Phys, 2016. **43**(2): p. 761-76.

46. Cirrone GAP, C.G., Mazzaglia SE, Romano F, Sardina D, Agodi C, Attili A, Blancato AA, De Napoli M, Di Rosa F, Kaitaniemi P, Marchetto F, Tarnavsky N, Tropea S, Zacharatou C. Harontherapy, *A Geant4-Based Tool for Proton/Ion-Therapy Studies.* Progress in NUCLEAR SCIENCE and TECHNOLOGY, 2011. **2**(207): p. 12.

47. Paganetti, H., *Range uncertainties in proton therapy and the role of Monte Carlo simulations.* Phys Med Biol, 2012. **57**(11): p. R99-117.

48. Paganetti, H., et al., *Clinical implementation of full Monte Carlo dose calculation in proton beam therapy.* Phys Med Biol, 2008. **53**(17): p. 4825-53.

49. Schumann, J., et al., *Efficient voxel navigation for proton therapy dose calculation in TOPAS and Geant4.* Phys Med Biol, 2012. **57**(11): p. 3281-93.

50. Testa, M., et al., *Experimental validation of the TOPAS Monte Carlo system for passive scattering proton therapy.* Med Phys, 2013. **40**(12): p. 121719.

51. Clavel, M.A., et al., *Validation of conventional and simplified methods to calculate projected valve area at normal flow rate in patients with low flow, low gradient aortic stenosis:*

the multicenter TOPAS (True or Pseudo Severe Aortic Stenosis) study. J Am Soc Echocardiogr, 2010. **23**(4): p. 380-6.

52. Zhu, X.R., et al., *Patient-specific quality assurance for prostate cancer patients receiving spot scanning proton therapy using single-field uniform dose.* Int J Radiat Oncol Biol Phys, 2011. **81**(2): p. 552-9.

53. Pedroni, E., et al., *The 200-MeV proton therapy project at the Paul Scherrer Institute: conceptual design and practical realization.* Med Phys, 1995. **22**(1): p. 37-53.

54. Lomax, A., *Intensity modulation methods for proton radiotherapy.* Phys Med Biol, 1999. **44**(1): p. 185-205.

55. Lomax, A.J., *Intensity modulated proton therapy and its sensitivity to treatment uncertainties 1: the potential effects of calculational uncertainties.* Phys Med Biol, 2008. **53**(4): p. 1027-42.

56. Lomax, A.J., et al., *Intensity modulated proton therapy: a clinical example.* Med Phys, 2001. **28**(3): p. 317-24.

57. Lomax, A.J., et al., *Treatment planning and verification of proton therapy using spot scanning: initial experiences.* Med Phys, 2004. **31**(11): p. 3150-7.

58. Zhu, X.R., et al., *Commissioning dose computation models for spot scanning proton beams in water for a commercially available treatment planning system.* Med Phys, 2013. **40**(4): p. 041723.

59. Chang, W.Y., C.C. Chiu, and J.H. Yang, *Block-Based Connected-Component Labeling Algorithm Using Binary Decision Trees.* Sensors (Basel), 2015. **15**(9): p. 23763-87.

60. Mackin, D., et al., *Improving spot-scanning proton therapy patient specific quality assurance with HPlusQA, a second-check dose calculation engine.* Med Phys, 2013. **40**(12): p. 121708.

61. Taylor, P.A., et al., *Results From the Imaging and Radiation Oncology Core Houston's Anthropomorphic Phantoms Used for Proton Therapy Clinical Trial Credentialing.* Int J Radiat Oncol Biol Phys, 2016. **95**(1): p. 242-8.

62. Lomax, A.J., et al., *A treatment planning inter-comparison of proton and intensity modulated photon radiotherapy.* Radiother Oncol, 1999. **51**(3): p. 257-71.

63. Weber, D.C., et al., *A treatment planning comparison of intensity modulated photon and proton therapy for paraspinal sarcomas.* Int J Radiat Oncol Biol Phys, 2004. **58**(5): p. 1596-606.

64. Newhauser, W.D. and R. Zhang, *The physics of proton therapy.* Phys Med Biol, 2015. **60**(8): p. R155-209.

65. J. Hartman, X.Z., X. R. Zhu, S.J. Frank, J.J.W. Lagendijk1, M. van Vulpen,and B.W. Raaymakers.

66. Emmert-Buck, M.R., et al., *Laser capture microdissection.* Science, 1996. **274**(5289): p. 998-1001.

67. Dean-Clower, E., et al., *Microdissection-based genetic discovery and analysis applied to cancer progression.* Cancer J Sci Am, 1997. **3**(5): p. 259-65.

68. Fend, F., et al., *Immuno-LCM: laser capture microdissection of immunostained frozen sections for mRNA analysis.* Am J Pathol, 1999. **154**(1): p. 61-6.

69. Keays, K.M., et al., *Laser capture microdissection and single-cell RT-PCR without RNA purification.* J Immunol Methods, 2005. **302**(1-2): p. 90-8.

70. Zhao, L., et al., *High-purity prostate circulating tumor cell isolation by a polymer nanofiber-embedded microchip for whole exome sequencing.* Adv Mater, 2013. **25**(21): p. 2897-902.

71. Chen, J.F., et al., *Subclassification of prostate cancer circulating tumor cells by nuclear size reveals very small nuclear circulating tumor cells in patients with visceral metastases.* Cancer, 2015. **121**(18): p. 3240-51.

Appendix

Table 0.1 Fluorescence intensity vs. Exposure Time

Fluorescence intensity vs. Exposure Time		
FITC	TRICY	Exposure Time（ms）
73.45	168.61	30
93.09	266.47	60
129.01	359.81	90
143.15	460.21	120
157.78	600	150
201.32	671	180
223.02	877	210
234.61	932	240
257	1009	270
278	1086	300
320	1150	330
346	1280	360
350	1456	390
390	1513	420
401	1762	450
426	1871	480
424	2011	510

441	2069	540
467	2130	570
481	2279	600
519	2866	720
574	3191	810
641	3258	900
725	3585	990

Copy right agreement

JOHN WILEY AND SONS LICENSE
TERMS AND CONDITIONS

Feb 27, 2017

This Agreement between Yang Zhang ("You") and John Wiley and Sons ("John Wiley and Sons") consists of your license details and the terms and conditions provided by John Wiley and Sons and Copyright Clearance Center.

License Number	4057220338591
License date	
Licensed Content Publisher	John Wiley and Sons
Licensed Content Publication	Cancer
Licensed Content Title	Subclassification of prostate cancer circulating tumor cells by nuclear size reveals very small nuclear circulating tumor cells in patients with visceral metastases
Licensed Content Author	Jie-Fu Chen,Hao Ho,Jake Lichterman,Yi-Tsung Lu,Yang Zhang,Mitch A. Garcia,Shang-Fu Chen,An-Jou Liang,Elisabeth Hodara,Haiyen E. Zhau,Shuang Hou,Rafi S. Ahmed,Daniel J. Luthringer,Jiaoti Huang,Ker-Chau Li,Leland W. K. Chung,Zunfu Ke,Hsian-Rong Tseng,Edwin M. Posadas
Licensed Content Date	May 14, 2015
Licensed Content Pages	12
Type of use	Dissertation/Thesis
Requestor type	Author of this Wiley article
Format	Electronic
Portion	Figure/table
Number of figures/tables	1
Original Wiley figure/table number(s)	Figure 3
Will you be translating?	No
Title of your thesis / dissertation	SEGMENTATION AND REGISTRATION BASED AUTOMATIC CANCER PROTON TREATMENT ANALYST
Expected completion date	May 2017
Expected size (number of	95

Permissions <permissions@iop.org> 2019年2月21日 上午4:14
收件人：Yang Zhang <zybf1208@gmail.com>

Dear Yang Zhang,

Thank you for your email and for taking the time to seek this permission.

When you transferred the copyright in your article to IOP, we granted back to you certain rights, including the right to include all or part of the Final Published Version of the article within any thesis or dissertation. Please note you may need to obtain separate permission for any third party content you included within your article.

Please include citation details, "© IOP Publishing. Reproduced with permission. All rights reserved" and for online use, a link to the Version of Record.

The only restriction is that if, at a later date, you wanted your thesis/dissertation to be published commercially, further permission would be required.

I wish you the best of luck with the completion of your thesis/dissertation.

Kind regards,

Christina

Copyright & Permissions Team
Gemma Alaway – Senior Rights & Permissions Adviser
Christina Colwell - Rights & Permissions Assistant

Contact Details
E-mail: permissions@iop.org

For further information about copyright and how to request permission: https://publishingsupport.iopscience.iop.org/copyright-journals/

See also: https://publishingsupport.iopscience.iop.org/

Please see our Author Rights Policy https://publishingsupport.iopscience.iop.org/author-rights-policies/

Please note: We do not provide signed permission forms as a separate attachment. Please print this email and provide it to your publisher as proof of permission.

Please note: Any statements made by IOP Publishing to the effect that authors do not need to get permission to use any content where IOP Publishing is not the publisher is not intended to constitute any sort of legal advice. Authors must make their own decisions as to the suitability of the content they are using and whether they require permission for it to be published within their article.

Curriculum Vita

Yang Zhang received his Bachelor of Engineering in Biotechnology in Harbin Institute of Technology in China, 2009. He earned his Master degree in Engineering from University of Texas at El Paso (UTEP) in 2012. Then, he joined the doctoral program in Biomedical Engineering at The University of Texas at El Paso under the supervision of Dr. Qian and work on dissertation "SEGMENTATION AND REGISTRATION BASED AUTOMATIC CANCER PROTON TREATMENT ANALYST".

Yang published several quality publication during his stay at UTEP. These include 12 journal, 3 peer reviewed conferences paper and 1 book Chapter. He worked as research assistant in Department of Civil Engineering. He also did intern as proton therapy fellow in M.D Anderson Cancer Center.

After graduation, he plans to work in medical device industry as a scientist.

Contact Email: zybf1208@gmail.com

This dissertation was typed by Yang Zhang